Supplementary information

Thermal Decomposition Pathways and Interfacial Reactivity in Potassium-Ion Batteries: Focus on Electrolyte and Anode

Siddhartha Nanda,[a] Andrei Dolocan,[a] Ayrton Yanyachi,[b] Saurabh Sandip Satpute,[c] Doosoo Kim,[a] Kami L. Hull,[c] Donal Finegan,[d] Ofodike Ezekoye,[b] Hadi Khani*[ab]

[a] *Materials Science & Engineering Program and Texas Materials Institute, The University of Texas at Austin, Austin, Texas 78712, USA.*

[b] *Walker Department of Mechanical Engineering, The University of Texas at Austin, Austin, TX 78712, USA.*

[c] *Department of Chemistry, The University of Texas at Austin, Austin, TX 78712, USA.*

[d] *National Renewable Energy Laboratory, Golden, CO, USA*

1. Experimental Methods

1.1. Electrochemical measurements

Full cells were assembled with a commercial graphite anode (2.1 mg cm^{-2}, film thickness ~ 90 µm, Na-carboxymethyl cellulose (Na-CMC) binders), a $K_xMn[Fe(CN)_6]_{1-y}\square_y \cdot nH_2O$ Prussian-blue analogue (PBA) type cathode,[1] and 2.5 M potassium bis(fluorosulfonyl)imide (KFSI; 98.9%, Sigma-Aldrich) in triethyl phosphate (TEP; 98.9%, Sigma-Aldrich) as the electrolyte. Circular electrodes (Ø 12.7 mm) were punched and placed in the vacuum-oven antechamber of an Ar-filled glovebox, then dried at 120 °C for 2 h under vacuum to remove moisture adsorbed during handling and transport. The negative-to-positive capacity ratio (N:P) was ~1.3, with average mass loadings of 3.1 mg cm^{-2} for the cathode and 2.1 mg cm^{-2} for the anode. To minimize corrosion from the KFSI-containing electrolyte, cells were assembled using Hohsen aluminum-coated coin cells. A Celgard separator was employed in all full cells to avoid loose-fiber contamination of the anode surface that could interfere with interfacial characterizations. Galvanostatic cycling was performed on a Neware battery tester. Cells underwent four formation cycles at 0.1 C within a 2.5–4.3 V window (vs. K^+/K). In the fifth cycle, each cell was brought to a target state of charge (0%, 50%, or 100% SOC) and then paused for subsequent thermal analysis, evolved-gas analysis, and interfacial characterization. For KIB benchmarking with carbonate electrolyte, analogous graphite half-cells were assembled using the same graphite electrode but employing 0.8 M KPF_6 in EC:DEC (1:1 by volume) as the electrolyte. To benchmark potassiated graphite anodes in KIBs against lithiated graphite anodes in LIBs, half-cells were assembled using single-sided graphite electrodes coated on copper foil (NEI Corporation). The electrode composition consisted of graphite, PVDF, and carbon black in a weight ratio of 90:5:5. The electrolyte used was 1 M $LiPF_6$ in a 1:1 volume ratio of ethylene carbonate (EC) and diethyl carbonate (DEC) (Sigma-Aldrich). Karl Fischer titration using a C20 Compact METTLER TOLEDO instrument was used to quantify the H_2O content of the electrolyte samples.

1.2. Sample preparation for thermal and gas analysis

The Cycled cells were decrimped in an Ar-filled glovebox and the wet electrode discs were retrieved. Because the discs carry an unknown amount of residual electrolyte, precise partitioning of electrode vs. electrolyte mass is not feasible. To ensure reproducible DSC responses, we applied a standardized three-stage wash-rinse-dry protocol to all harvested anodes. Briefly, as-harvested

(wet) electrodes were immersed in dimethyl carbonate (DMC, ≥99.9%, H_2O <10 ppm) for 10 min (*wash*), then transferred to a second vial containing fresh DMC for an additional 10 min (*rinse*) to remove surface electrolyte/salt. Washed electrodes were then placed overnight under vacuum at ambient temperature in the glovebox antechamber to remove residual DMC (*dry*). For thermal and gas-analysis measurements, ~4–6 mg of anode powder was scraped from the prepared discs and loaded into either a high-pressure, 30-µL gold-plated stainless-steel crucible (for HP-DSC) or a 40-µL aluminum crucible (for DSC–TGA–MS–FTIR). Depending on the experiment, fresh electrolyte, KFSI salt, or TEP solvent was added to the anode powder at a 1:1 mass ratio, gently mixed, and pressed to the bottom of the crucible. All steps, from decrimping and wash-rinse-dry to sample loading and crucible sealing, were performed inside the Ar-filled glovebox. Crucibles were sealed using the appropriate Mettler Toledo sealing presses and then transferred out of the glovebox for analysis.

1.3. Thermal and gas characterizations

HP-DSC and TGA/DSC measurements were performed on METTLER TOLEDO DSC 3+ and TGA/DSC 3+ instruments, respectively, using STARe software. Reported heat-flow values were normalized to sample mass. After loading, the TGA furnace was purged with N_2 for 10 min at 150 mL min^{-1}. The heating rate was 10 °C min^{-1} from 25 to 600 °C for TGA/DSC and from 25 to 340 °C for HP-DSC. The gas flow rate of 50 mL min^{-1} of UHP Nitrogen that was pass through a molecular sieved prior to entering TGA/DSC or DSC furnaces was used. For TGA/DSC, samples were weighed into aluminum crucibles, hermetically sealed with cold-pressed lids inside the glovebox, then transferred to the TGA/DSC autosampler located outside the glovebox; immediately before insertion into the furnace, the robotic autosampler pierced each lid at the dedicated piercing station to create a small vent hole, minimizing sample exposure during the wait period and enabling controlled gas exchange for gas-evolution and thermogravimetric analyses.

Electron-ionization mass spectrometry (EI–MS) was performed using a Hiden Analytical HPR-20 R&D gas-analysis system equipped with a HAL/3F 201 RC triple-filter quadrupole (1–200 amu) and dual detectors (Faraday cup and secondary-electron multiplier); the system included the corrosion-resistant upgrade (platinum ionizer and corrosive-gas-resistant seals). The instrument was coupled to the DSC/TGA via the QIC interface, which delivers ~200 µL min^{-1} and is equipped with a heating jacket that maintains the temperature at 110 °C to prevent condensation.

The ion source was operated at 70 eV with an analyzer pressure of ~2 × 10^{-6} Torr. For data acquisition, m/z 1-45 were recorded on the Faraday detector (approximate detection limit 10^{-5}–10^{-10} mbar), and m/z 46-200 on the SEM detector (approximate detection limit 10^{-7}-10^{-14} mbar). A Nicolet iG-50 FTIR was operated in parallel with EI-MS via a three-way valve. During TGA-DSC measurements, evolved gases were carried by UHP N_2 (150 mL min^{-1}) through the FTIR; the stream was split, with a portion going to exhaust and the remainder passed through a -12 °C cold trap to the EI-MS to prevent detector saturation (**Figure S1a**). After each run, purging was performed (N_2, 150 mL min^{-1}, ~30 min) until a flat baseline was achieved. The SO_2 and HF gas quantification using the TGA-FTIR setup was conducted according to our previous report.[2] Gas chromatography mass spectroscopy (GC-MS) of thermally treated electrolyte was performed using a Shimadzu single-quadrupole GC-MS. Raman spectra were conducted on a HORIBA LabRAM HR Evolution using a 532 nm excitation laser and a 600 lines mm^{-1} grating over 50-3200 cm^{-1}.

1.4. Surface characterizations

To analyze the near-surface (<7 nm) chemical composition of the SEI, X-ray photoelectron spectroscopy (XPS, Kratos AXIS Ultra DLD) was employed. After cycling, anode discs were harvested from full cells, then washed, rinsed, and dried in an Ar-filled glovebox to minimize residual electrolyte, enabling isolation of thermally induced transformations in the SEI and underlying graphite. Anode samples were heated at 10 °C min^{-1} to 110 or 340 °C in a box furnace located inside the glovebox, held for 10 min, and then allowed to cool to ambient temperature. All handling and transfers were performed under inert conditions; cooled samples were placed in an Ar-filled sealed transfer capsule (airtight sample holder) and transported to the XPS instrument without air exposure (see **Figure S18** for the complete workflow). The XPS spectra were charge-corrected by referencing the C 1s C–C peak to 285 eV. Spectral deconvolution was performed using CasaXPS software with a Shirley background. The full width at half maximum (FWHM) for each fitted peak component was constrained between 1.0 and 2.0 eV. For doublet peaks, spin–orbit splitting and area constraints were applied as follows: phosphorus (P 2p) doublets were fit with a fixed binding energy separation of 0.86 ± 0.05 eV and a 2:1 area ratio (3/2:1/2), while sulfur (S 2p) doublets were fit with a separation of 1.18 ± 0.05 eV and the same 2:1 area ratio. The FWHM of the two peaks in each doublet was constrained to be equal.

An M6 ToF-SIMS instrument (IONTOF GmbH, 2023) was used for depth profiling.The system was equipped with a Bi^+ analysis gun (30 kV, ~0.3 pA), dual sputter guns (Cs^+ and O_2^+, ~40 nA at 0.5 kV and 1 kV, respectively), and a Ga^+ FIB column (20 kV, 20 nA). During depth profiling, the Bi^+ analysis beam was raster-scanned over 100 µm × 100 µm, while the sputter beam (Cs^+ or O_2^+) was raster-scanned over 300 µm × 300 µm concentric to the analysis area. Depth profiles were acquired in non-interlaced mode, that is, sequential analysis and sputtering. Negative secondary ions were collected during Cs^+ sputtering and positive ions during O_2^+ sputtering. The mass resolution exceeded 5000 (m/Δm). Data acquisition was performed in ultra-high vacuum at a base pressure of ~1×10^{-9} mbar. Samples were prepared and transferred from the Ar-filled glovebox to the ToF-SIMS load lock using an air-free sealed capsule; the glovebox-to-instrument transfer procedure matched that used for XPS. Data statistics were computed with an in-house script in Igor Pro 8 (WaveMetrics, Inc.). For this study, ToF-SIMS depth profiling was used to identify, localize, and relatively quantify secondary-ion fragments representative of SEI species. SEI depth was estimated from sputter time using a graphite sputter-rate calibration under the stated conditions, where 1 s of sputtering corresponds to ~0.04 nm of removed material.[3] Unless noted, the analysis raster was 100 µm × 100 µm in the x-y plane with a total profiled depth of ~160 nm.

An operational thickness for a given species was defined from its normalized depth profile using a 0.60-of-maximum threshold. Specifically, the thickness equals the distance between the two depths where the normalized intensity crosses 0.60 on the rising and falling edges. For a near-Gaussian profile this interval approximates the ±1σ bounds, which contain ~68 % of the profile area. Relative abundances were estimated by integrating the raw secondary-ion intensity between these two 0.60 intersections and normalizing to the maximum raw intensity of the graphite reference signal (C_6^-). This internal normalization reduces matrix and instrumental variability while enabling comparison across samples run under identical beam conditions.

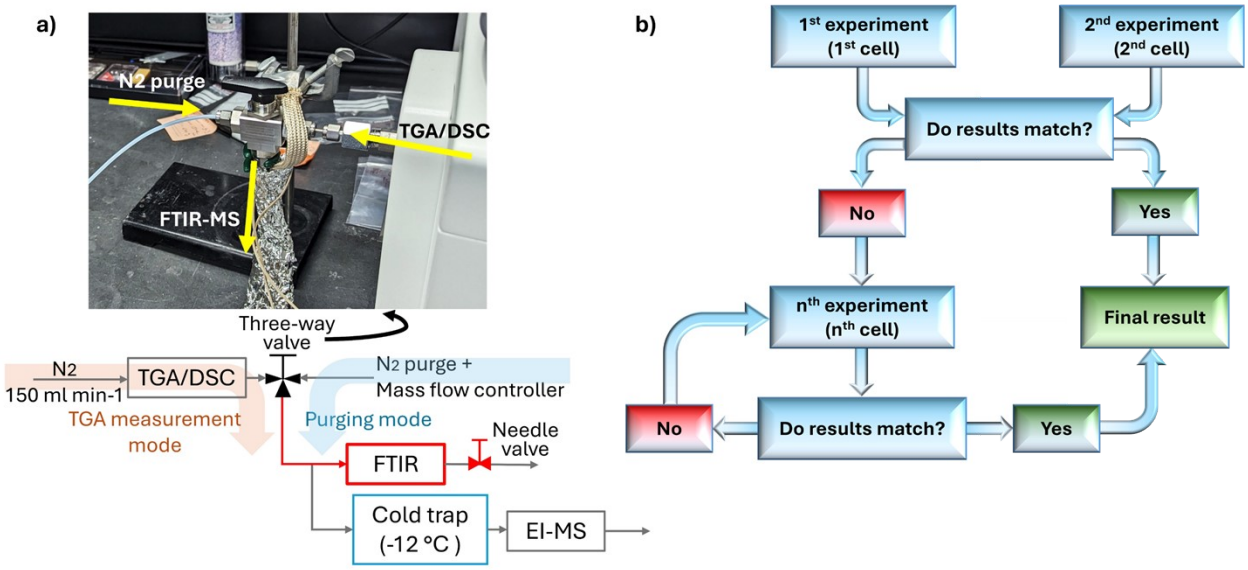

Figure S1. (a) In-house built three-way valve mechanism for connecting TGA-DSC to FTIR and MS for evolved gas analysis, (b) Schematic illustrating the strategy for ensuring performance consistency and repeatability in TGA-DSC and HP-DSC measurements.

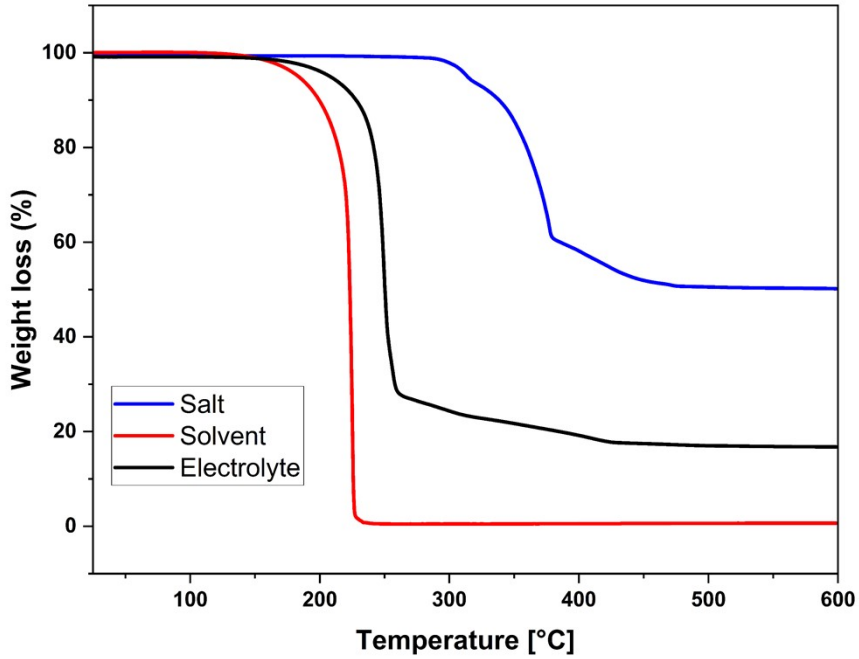

Figure S2. TGA for salt (KFSI), solvent (TEP), and electrolyte (2.5 M KFSI in TEP) showing mass loss of 48.5%, 99.5%, and 82.0% respectively.

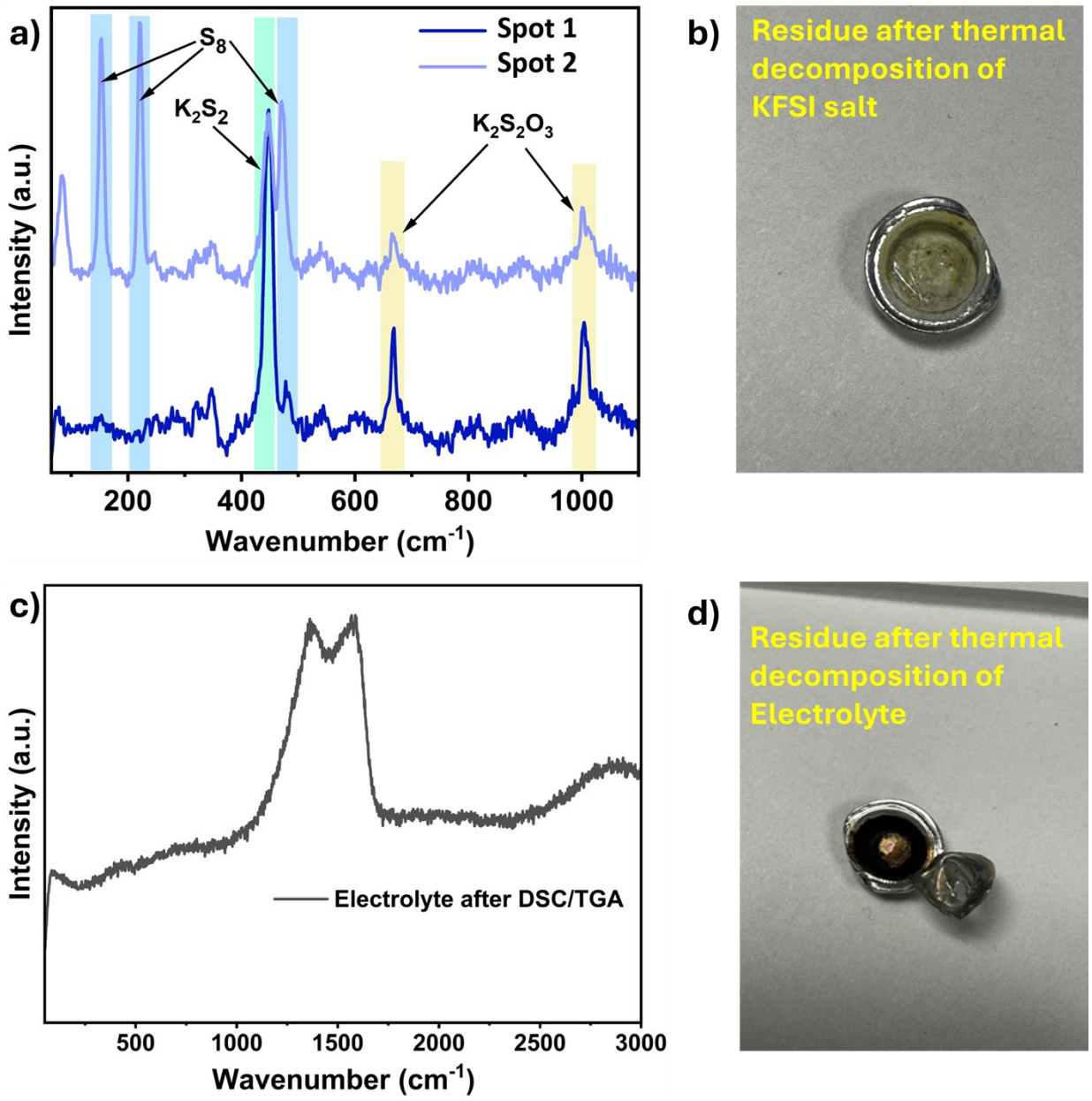

Figure S3. (a) Raman spectra collected at two different spots on the residue remaining after TGA-DSC analysis of KFSI. (b) Visual appearance of KFSI residue following thermal treatment. (c) Raman spectra of the residue obtained after TGA-DSC analysis of the electrolyte. (d) Black residue observed after thermal treatment of the electrolyte.

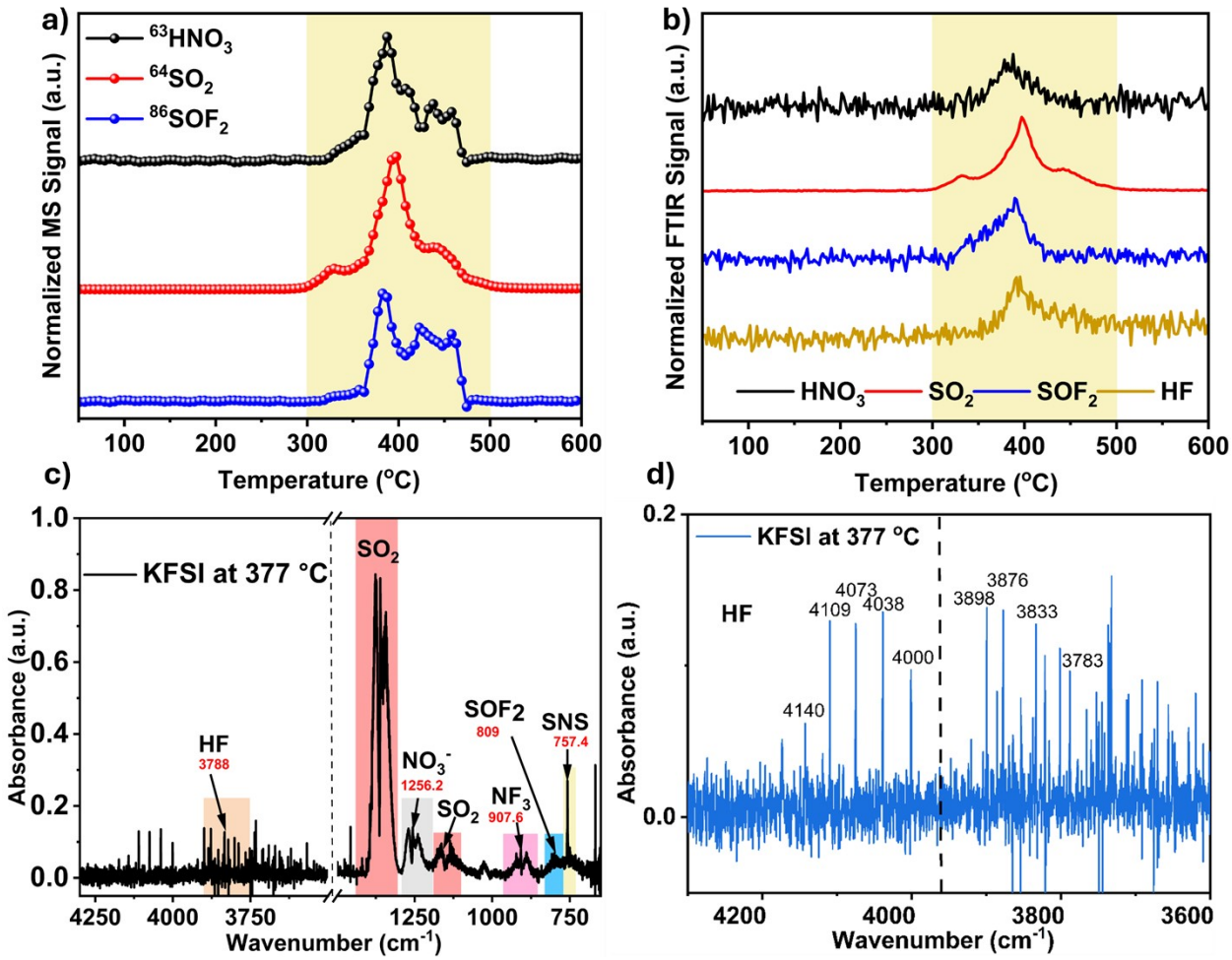

Figure S4. (a) Mass spectrometry (MS) signal of gases evolved from KFSI during thermal analysis. (b) FTIR spectra of gases released from KFSI. (c) Complete FTIR spectrum at 377 °C for KFSI decomposition. (d) Enlarged FTIR region highlighting HF absorption peaks.

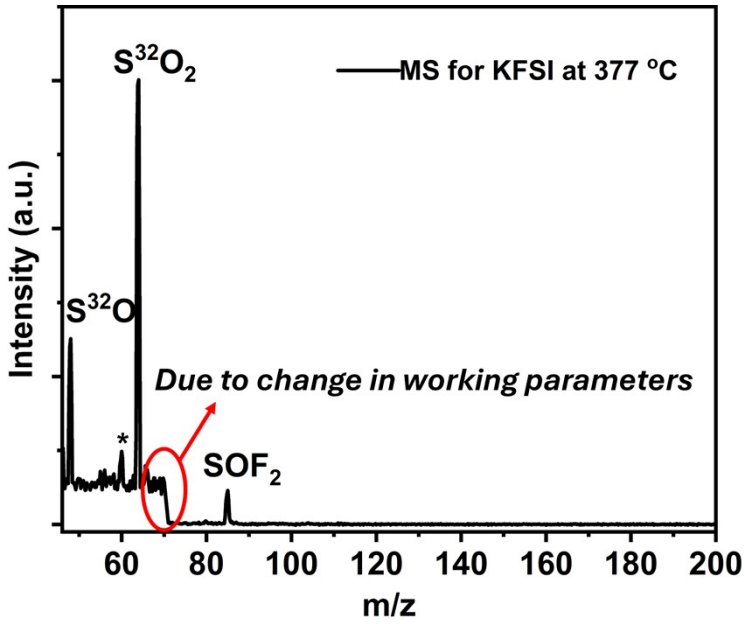

Figure S5. *m/z* versus intensity plot for KFSI at 377 °C, indicating the presence of gaseous species such as SO_2 and SOF_2. The observed intensity jump results from two separate scanning ranges: one from *m/z* = 45–70 and another from *m/z* = 71–200.

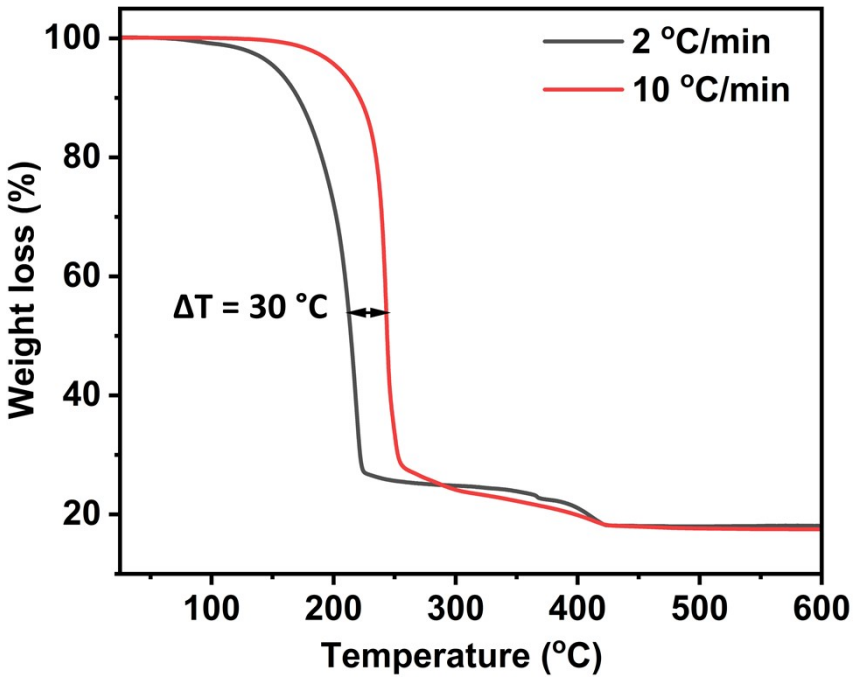

Figure S6. TGA profiles for the electrolyte performed at different heating rates, showing a 30 °C shift in the onset temperature of the major thermal event.

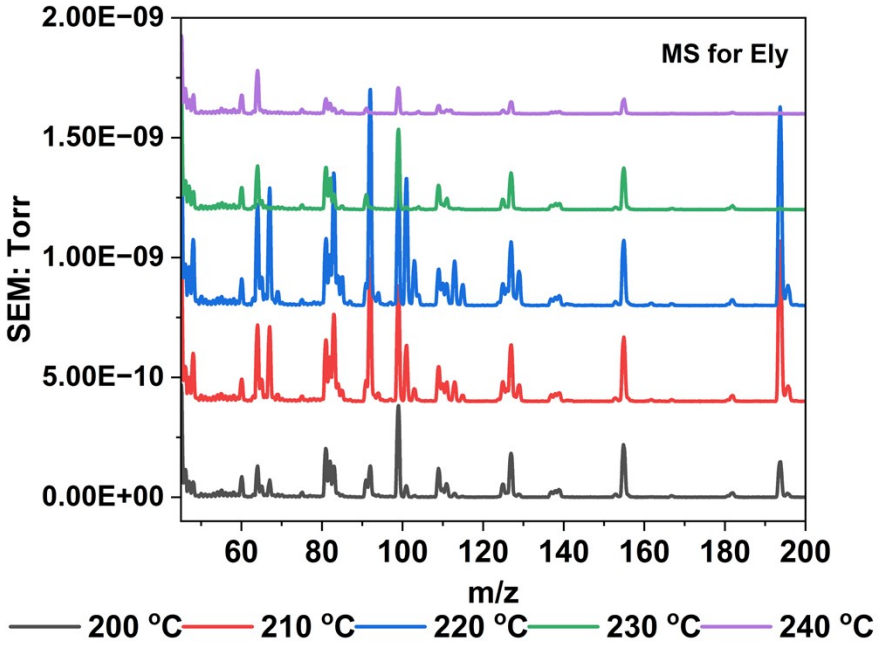

Figure S7. *m/z* versus intensity (pressure inside the SEM chamber in Torr) at five different temperatures during the electrolyte heating schedule, showing progressive gas evolution. Detected species include ethanol (*m/z* = 45), SO_2 (*m/z* = 64), TEP (*m/z* = 99, 155), diethyl fluorophosphate (DEFP, *m/z* = 101), and ethylsulfonyl fluoride (ESF, *m/z* = 194).

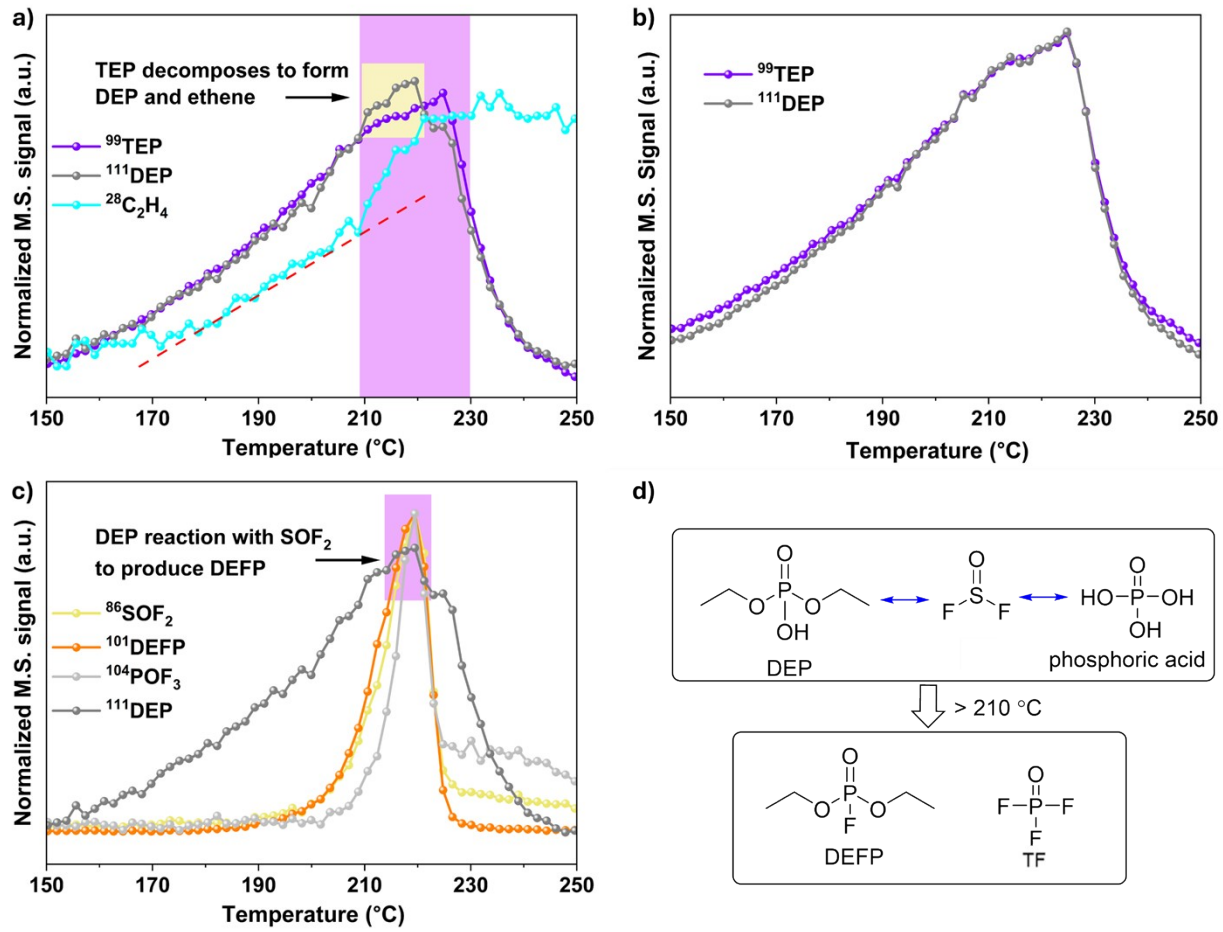

Figure S8. (a) MS profiles highlighting thermal decomposition of TEP into DEP and ethene within the electrolyte, evidenced by increasing DEP intensity and decreasing TEP intensity in the shaded yellow region. (b) Overlapping MS profiles of DEP and TEP confirming no decomposition when TEP is present alone under thermal treatment. (c) Reaction of DEP with SOF_2 leading to formation of diethyl fluorophosphate (DEFP). (d) Schematic illustrating the proposed mechanism for DEP and H_3PO_4 reacting with SOF_2 to generate DEFP and POF_3.

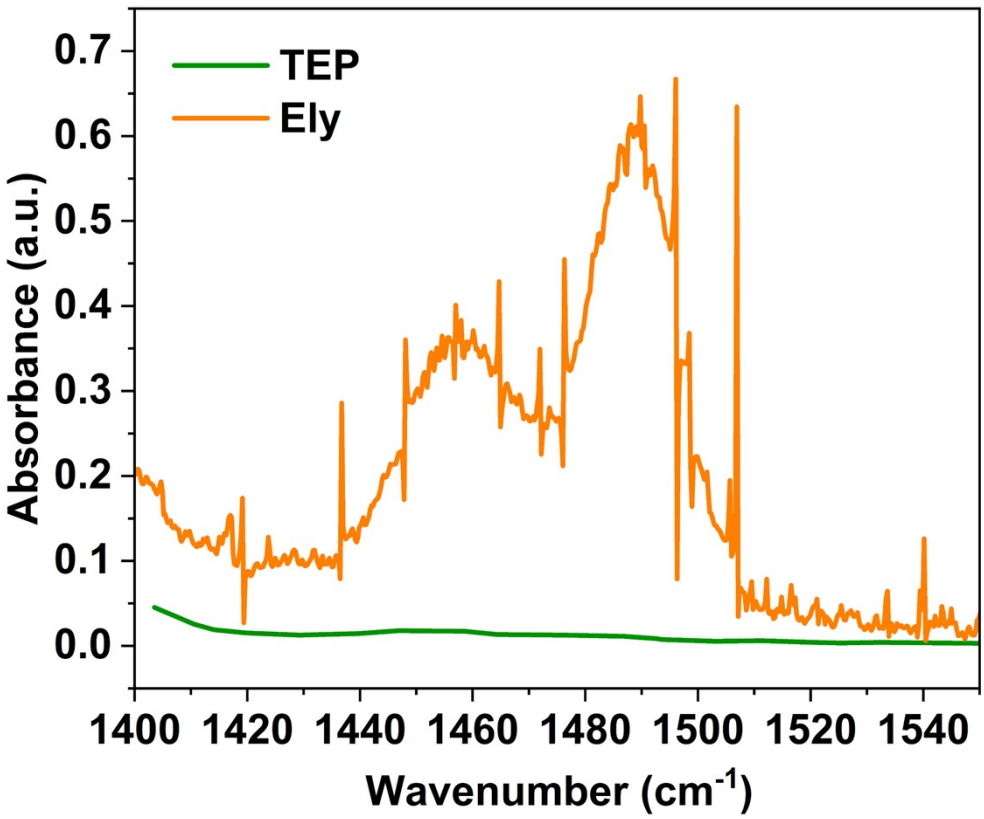

Figure S9. Enlarged FTIR region (1400-1550 cm^{-1}) showing the presence of characteristic peaks for various gases evolved from TEP and electrolyte at 250 ºC in TGA-DSC.

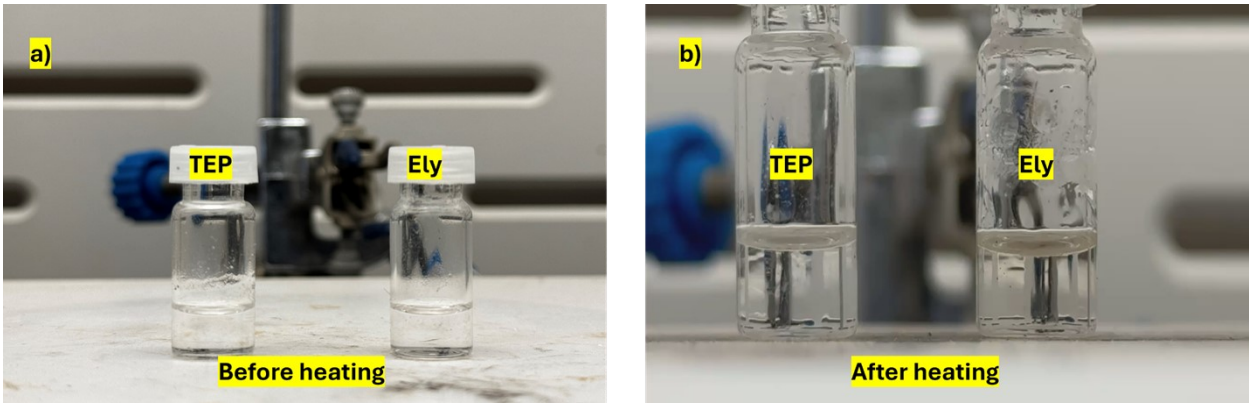

Figure S10. Thermal treatment of TEP and electrolyte (Ely) on a hot plate maintained at 250 °C, sealed in GC–MS vials. A distinct color change observed in the electrolyte (b) indicates thermal decomposition, whereas TEP remains visually unchanged.

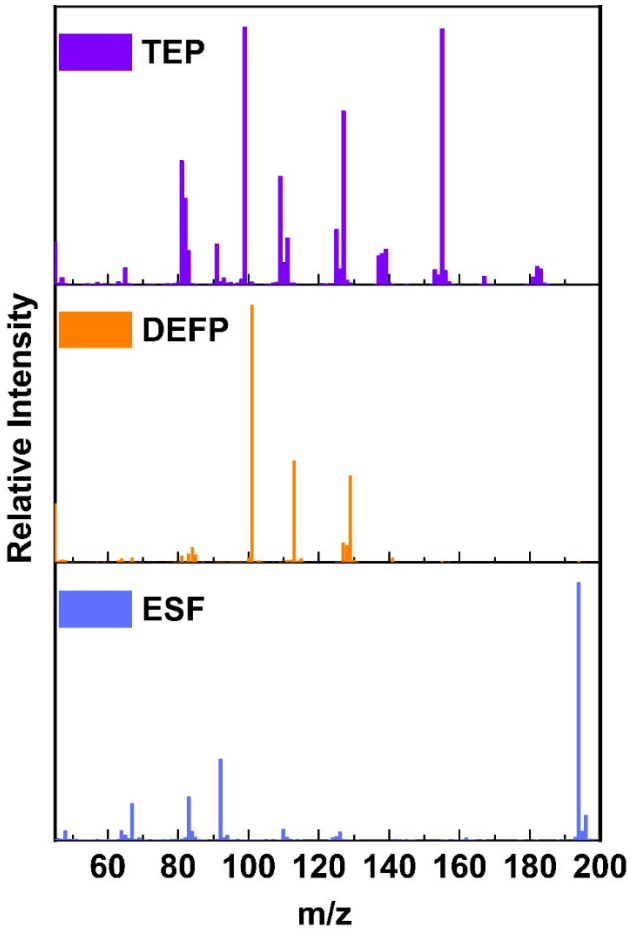

Figure S11. Fragmentation patterns for three compounds identified by GC–MS after thermal treatment of the electrolyte at 250 °C: triethyl phosphate (TEP, top), diethyl fluorophosphate (DEFP, middle), and ethane-1,2-disulfonyl difluoride (ESF, bottom).

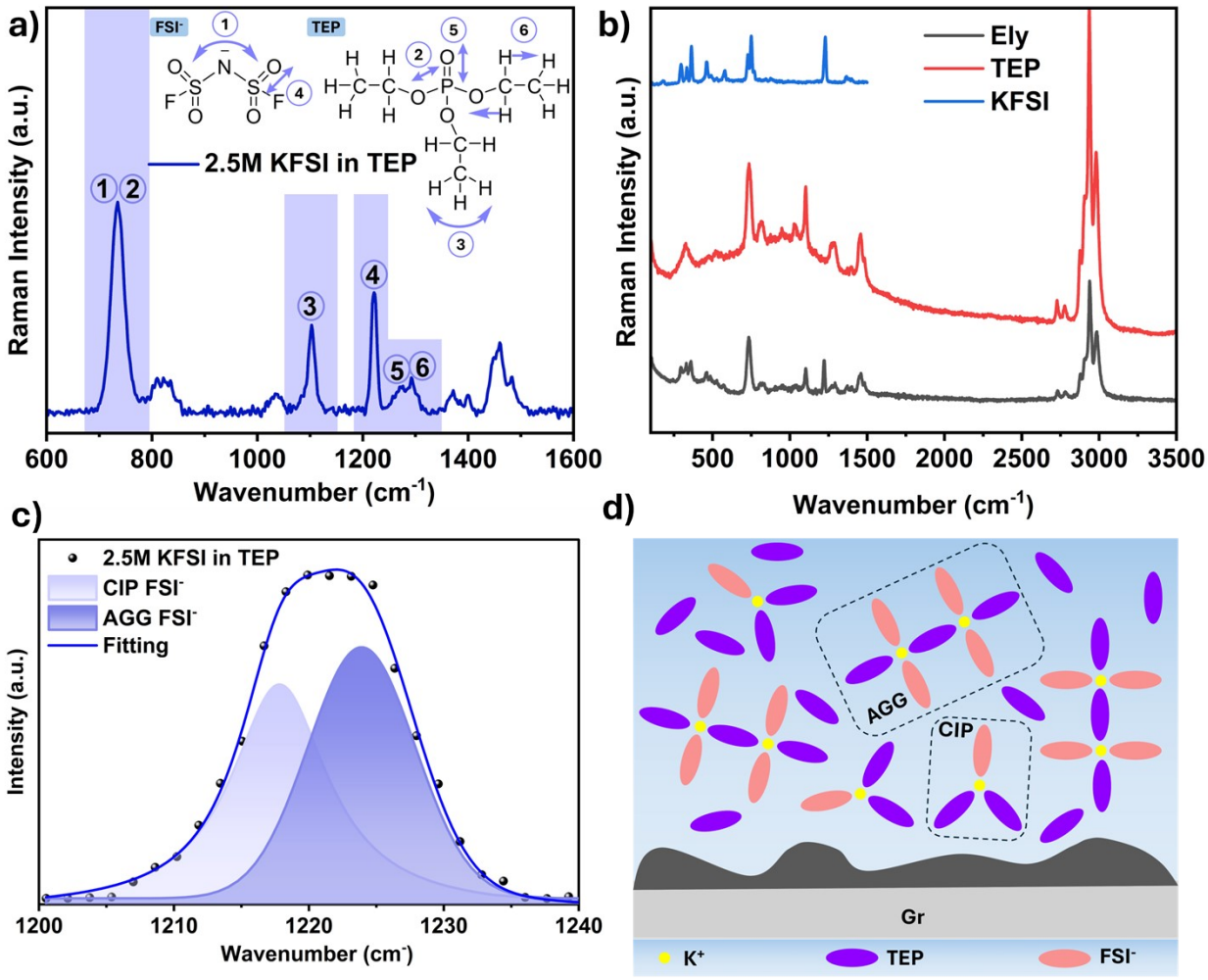

Figure S12. (a) Raman spectrum for 2.5M KFSI in TEP with insets showing different bond vibrations, (b) Raman spectrum of KFSI, TEP, and the electrolyte, (c) Voigt fitting of the S=O Raman peak (1200-1240 cm^{-1}) with insets illustrating molecular arrangements for contact ion pairs (CIPs) and aggregates (AGGs). (d) Proposed schematic of the solvation structure.[4]

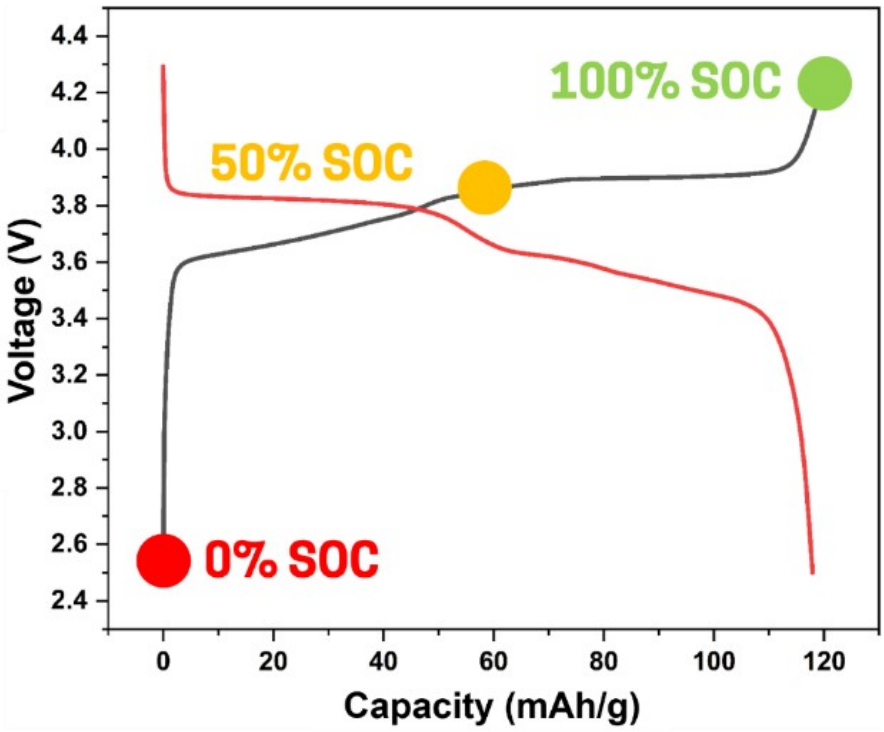

Figure S13. Galvanostatic charge–discharge (GCD) profile at the 4th cycle for a K-ion full cell (see Experimental Methods for full configuration). The measurement was performed at 0.1 C within 2.5–4.3 V (vs. K^+/K), delivering a capacity of ~0.5 mAh (~120 mAh g^{-1}). Cycling was stopped at selected states of charge (SOCs), and the retrieved anodes were subsequently analyzed for gas evolution, thermal behavior, and interfacial characteristics.

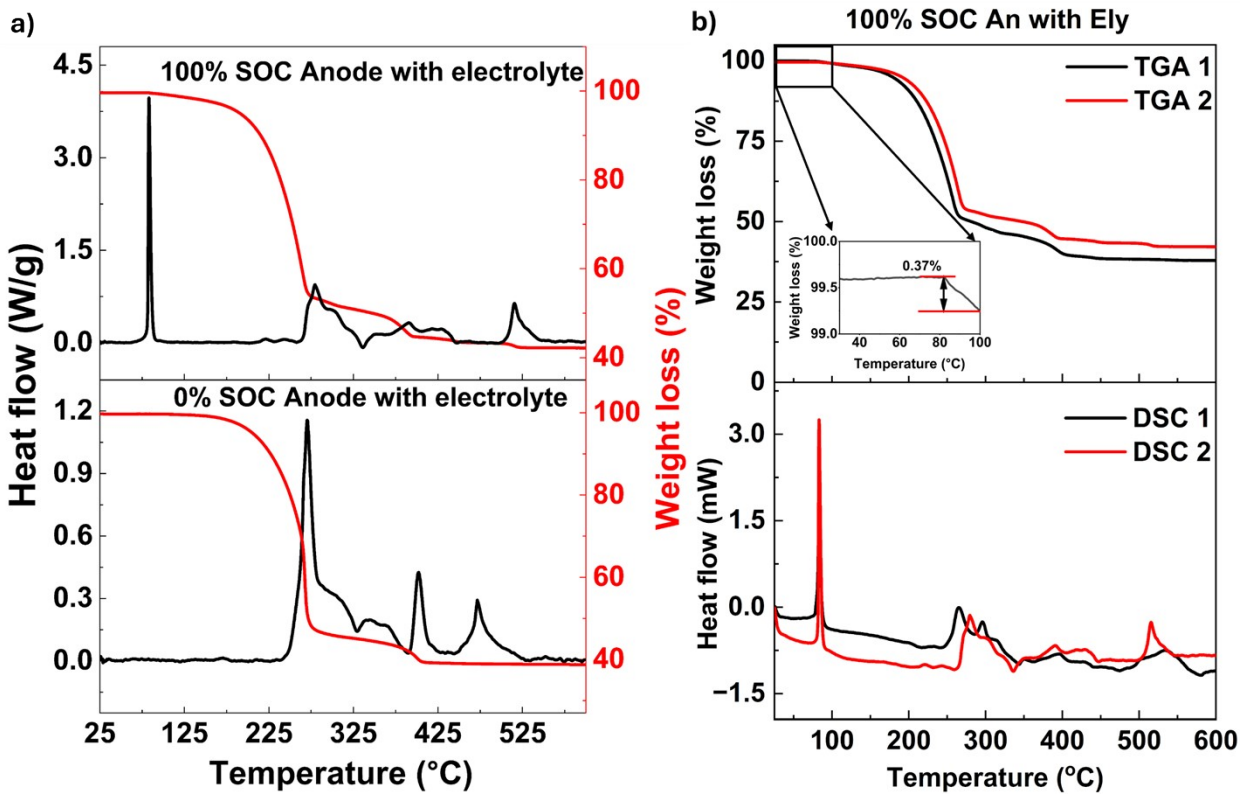

Figure S14. (a) DSC–TGA profiles for potassiated anodes with electrolyte at 0% and 100% SOC. (b) Repeatability tests for DSC–TGA on 100% SOC anodes with electrolyte (without baseline correction), showing that peak temperatures for the major exothermic event are closely aligned (within ~10 °C). TGA results are also consistent, with only a ~5 wt% difference. Inset in (b) indicates minimal mass loss (0.37%) below 100 °C.

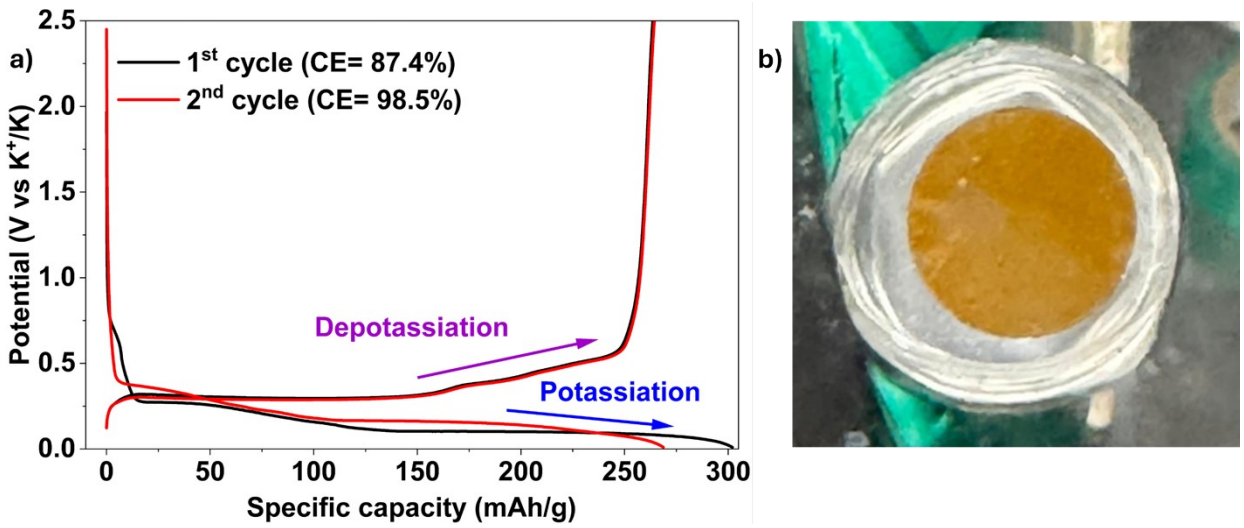

Figure S15. (a) Galvanostatic charge–discharge (GCD) data for two cycles of K–graphite (K–Gr) half-cells. The first-cycle charge (depotassiation) capacity is 264 mAh g^{-1}, close to the theoretical capacity of 279 mAh g^{-1} for fully intercalated KC_8. The first-cycle discharge capacity is 302 mAh g^{-1}, exceeding the theoretical value due to irreversible capacity loss from SEI formation. Despite this, the first-cycle coulombic efficiency (CE) using 2.5 M KFSI in TEP electrolyte is 87.4%, significantly higher than previously reported K–Gr half-cells cycled in 1 M KPF_6 in EC:PC (1:1 by vol%) (~66.5%),[5] indicating improved SEI stability in the investigated system. The second cycle delivers an outstanding CE of 98.5%. (b) Photograph of the extracted graphite anode at 100% SOC (KC_8), showing a yellow coloration indicative of full potassiation.

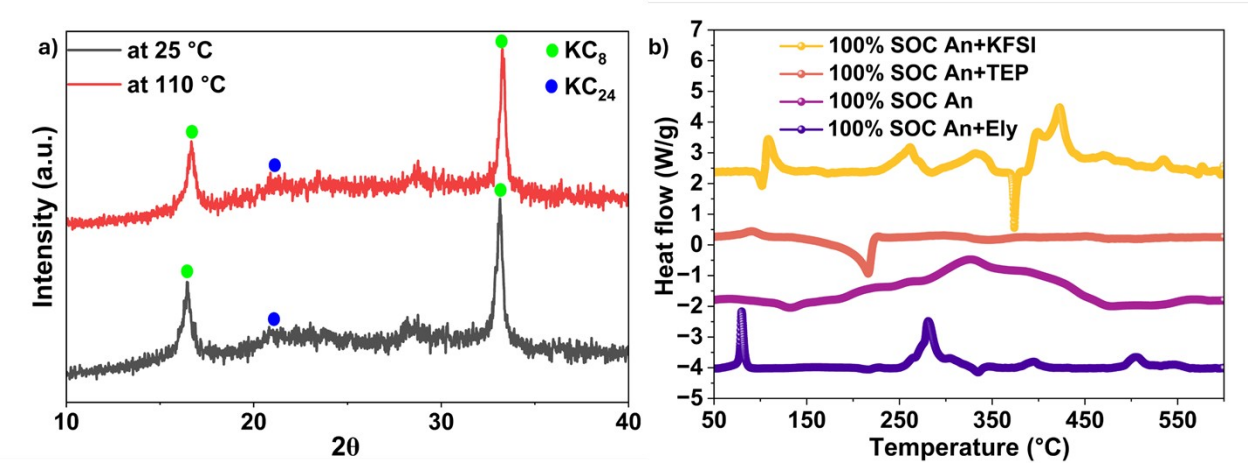

Figure S16. (a) XRD patterns of graphite anodes at 100% SOC under two conditions: (i) washed and dried, and (ii) washed, dried, and heated at 110 °C. (b) Full DSC–TGA spectra for controlled experiments on 100% SOC anodes with KFSI, TEP, electrolyte and 100% SOC anode (washed and dried) analyzed separately to identify the origin of low-temperature exothermic events.

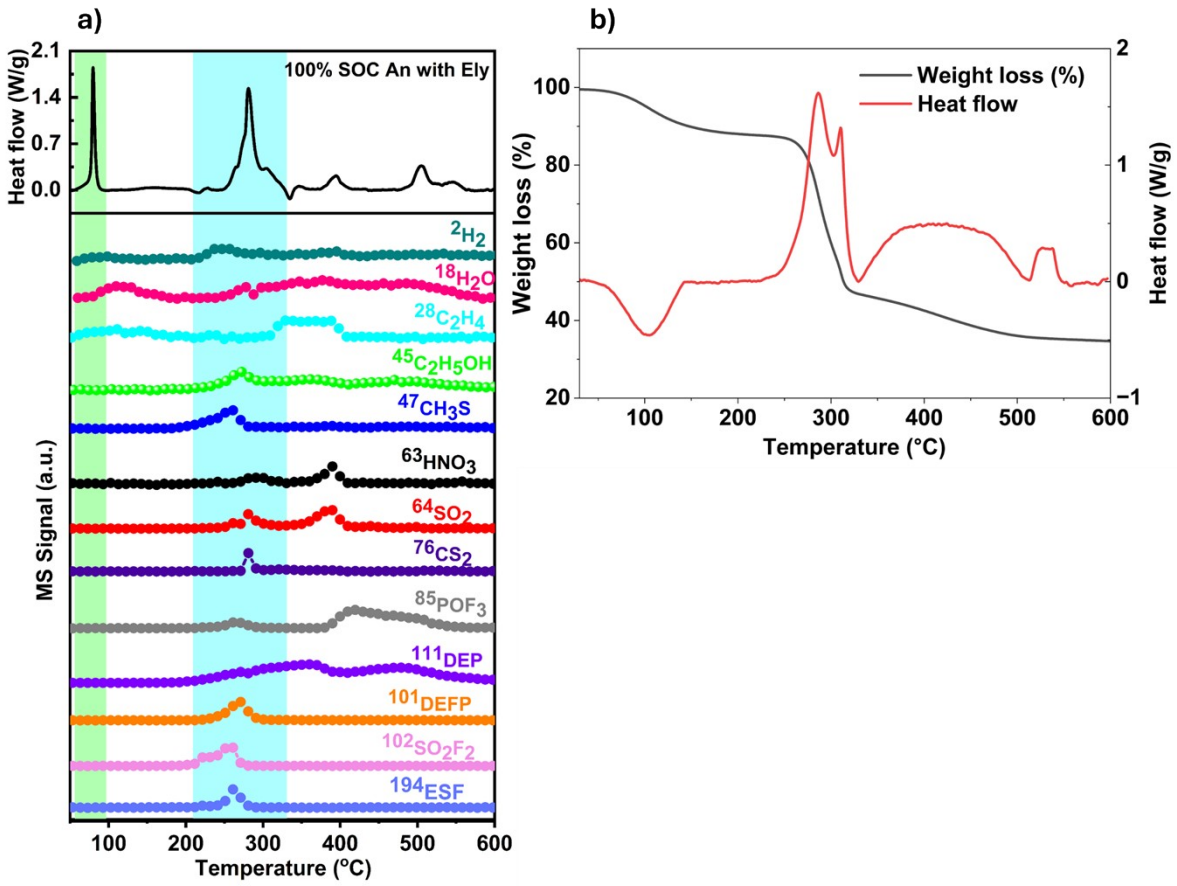

Figure S17. (a) Complete DSC–MS profiles showing all gases evolved during thermal treatment of a 100% SOC anode with electrolyte over the temperature range of 25–600 °C, (b) DSC–TGA measurement of Na-CMC binder.

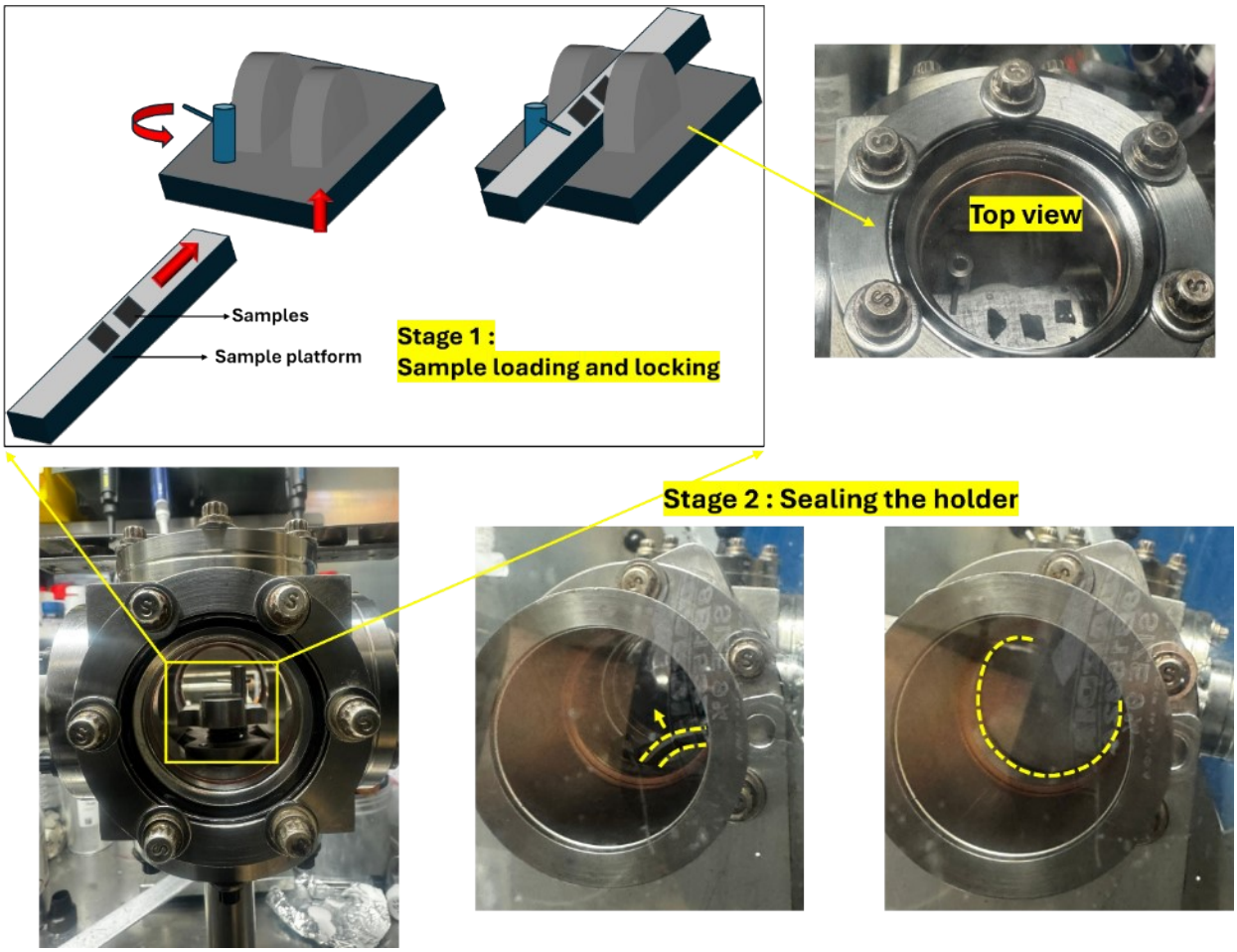

Figure S18. Sample loading and transfer procedure for XPS measurements. The chamber interior is equipped with a locking mechanism for securing the sample holder. As illustrated in the schematic, anode pieces (cut from anode discs) are first mounted on a stainless-steel rectangular bar using carbon tape. This bar is then placed on a movable platform, while a rotating knob with a pin locks the bar from above. Finally, the chamber is sealed with a door as shown. All steps are performed inside a glovebox to prevent air exposure and ensure sample integrity.

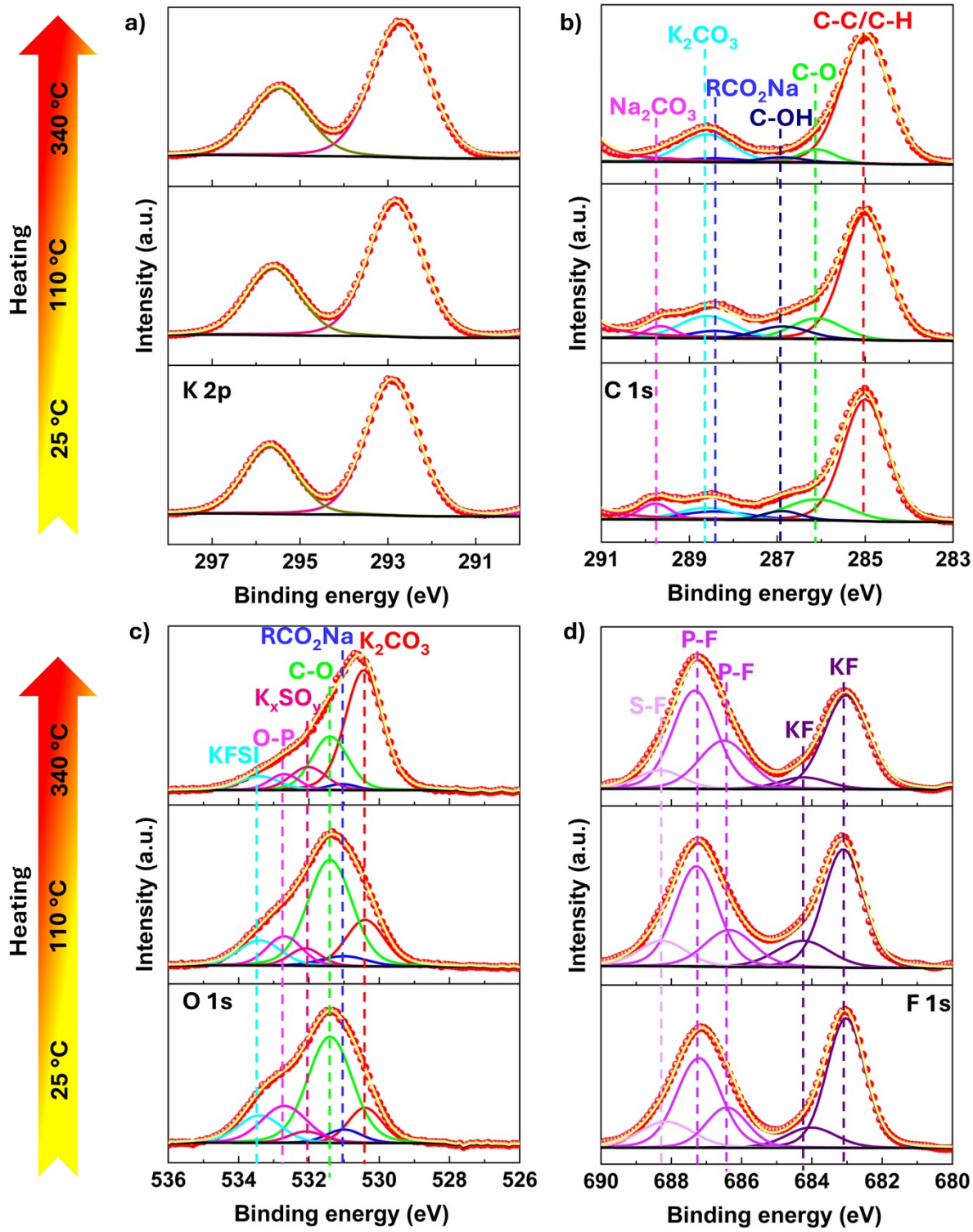

Figure S19. XPS spectra of (a) K 2p, (b) C 1s, (c) O 1s, and (d) F 1s regions collected at three different temperatures, illustrating changes in chemical states with thermal treatment.

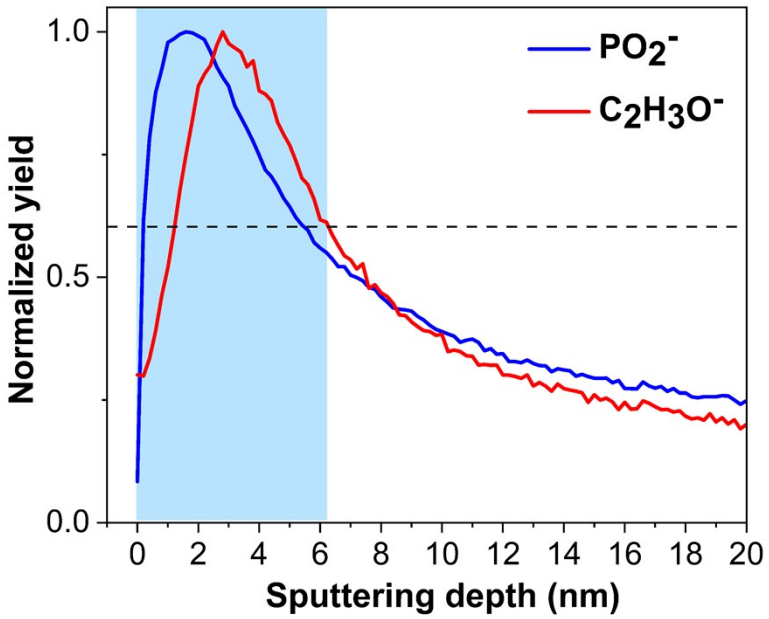

Figure S20. Normalized depth profiles for two fragments, $C_2H_3O^-$ and PO_2^-, confirming the presence of partially potassiated organic species such as $(C_2H_5O)_2PO(OK)$ and $(C_2H_5O)PO(OK)_2$ in the outer SEI layer (<6 nm).

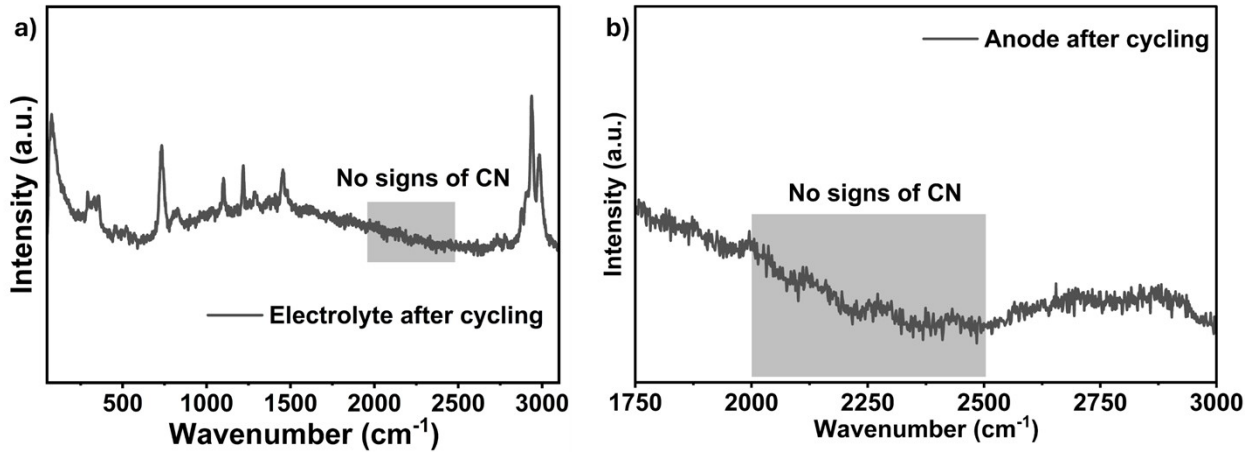

Figure S21. Raman spectra of (a) the electrolyte and (b) the anode retrieved from a cycled coin cell, analyzed to investigate the presence of cyanide (CN) species, whose characteristic Raman modes typically appear in 2000-2200 cm^{-1} region.

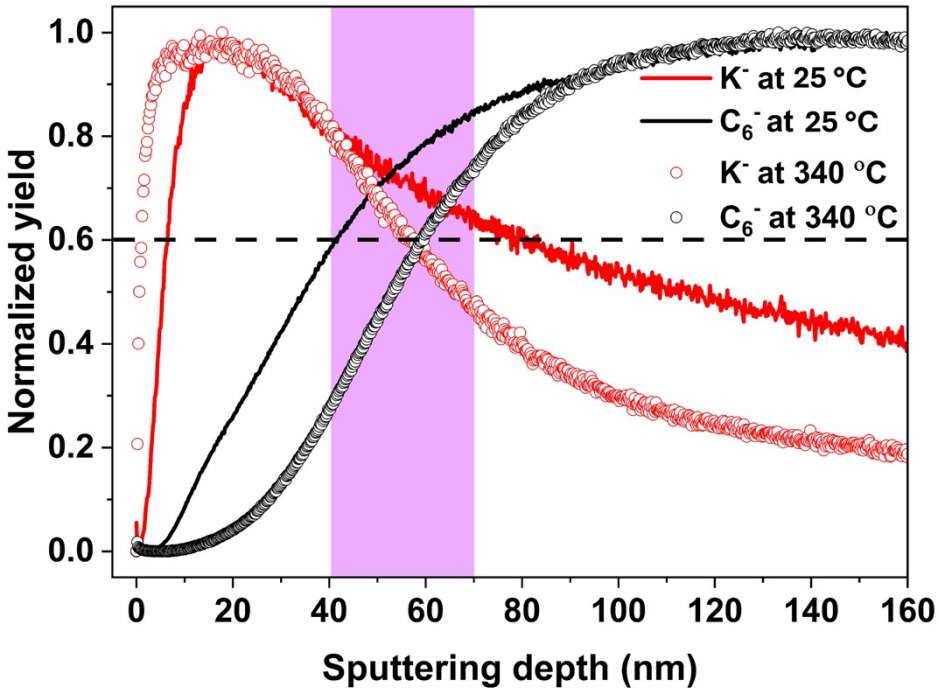

Figure S22. Normalized ToF-SIMS depth profiles for K^- and C_6^- in a 100% SOC potassiated graphite anode, measured before thermal treatment (25 °C) and after thermal treatment (340 °C). The profiles illustrate K^+ outward migration, graphite layer contraction, and the formation of a K^+ concentration depletion region.

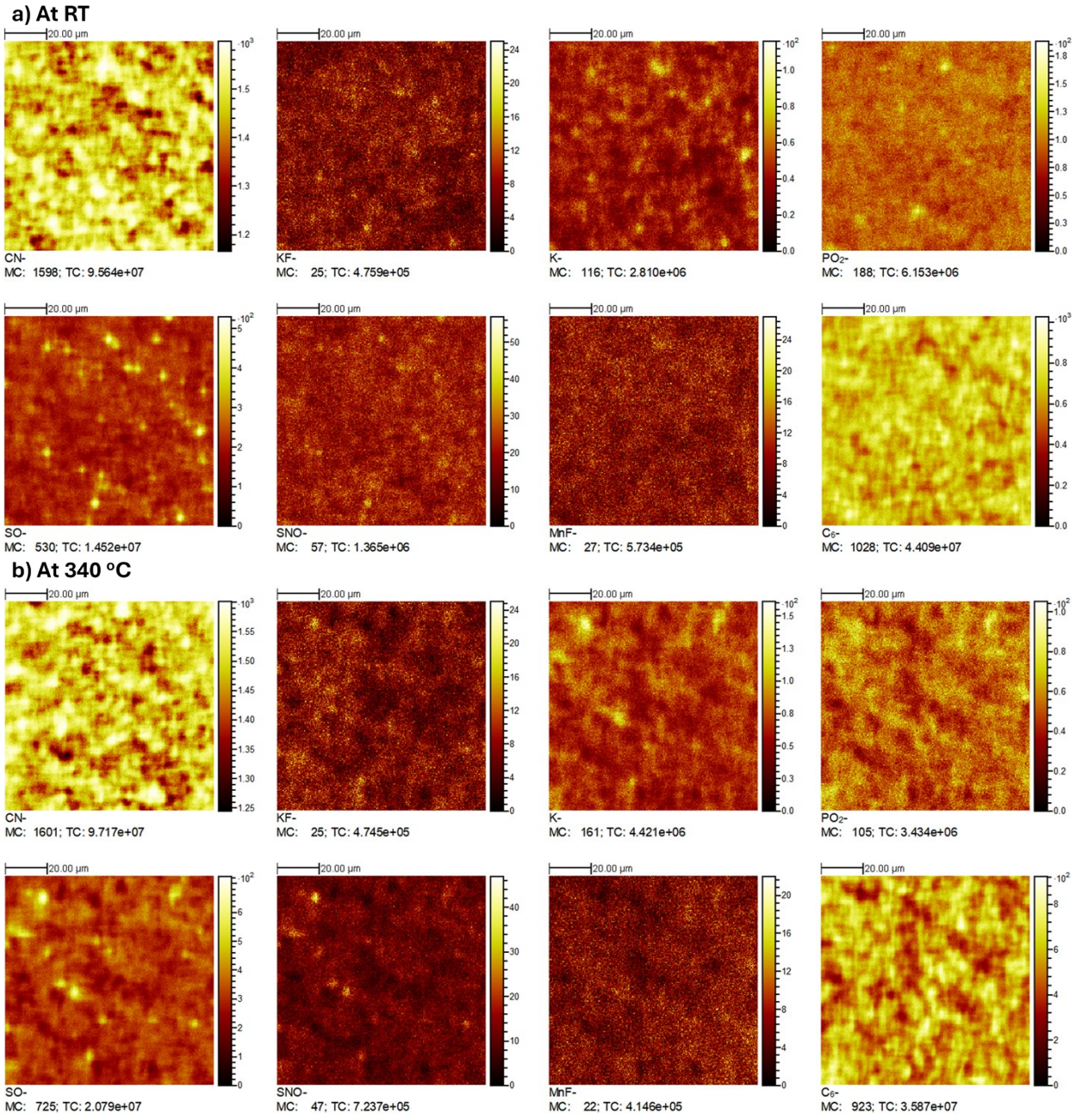

Figure S23. Total yield maps for selected ion fragments at (a) 25 °C (room temperature, RT) and (b) 340 °C, illustrating changes in fragment distribution with thermal treatment.

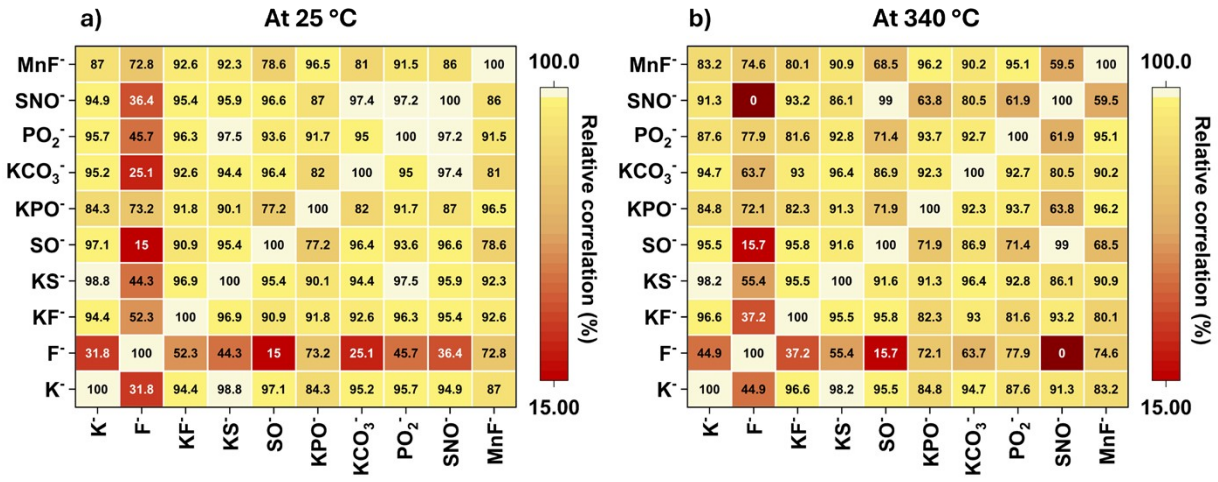

Figure S24. Relative correlation matrices of selected ion fragments from cycled anodes at (a) 25 °C and (b) 340 °C. Color scale bars represent spatial correlation probability (%).

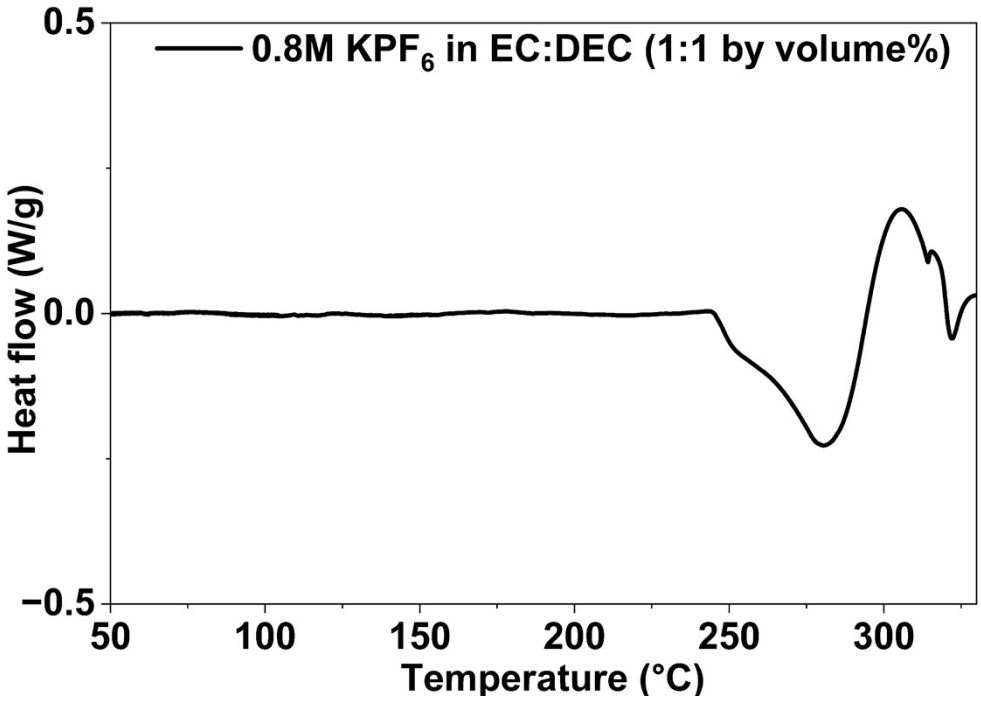

Figure S25. HP-DSC measurements for 0.8 M KPF_6 in EC:DEC (1:1 by volume) showing the onset of thermal decomposition near ~250 °C with a total heat of ~ 41 J g^{-1}.

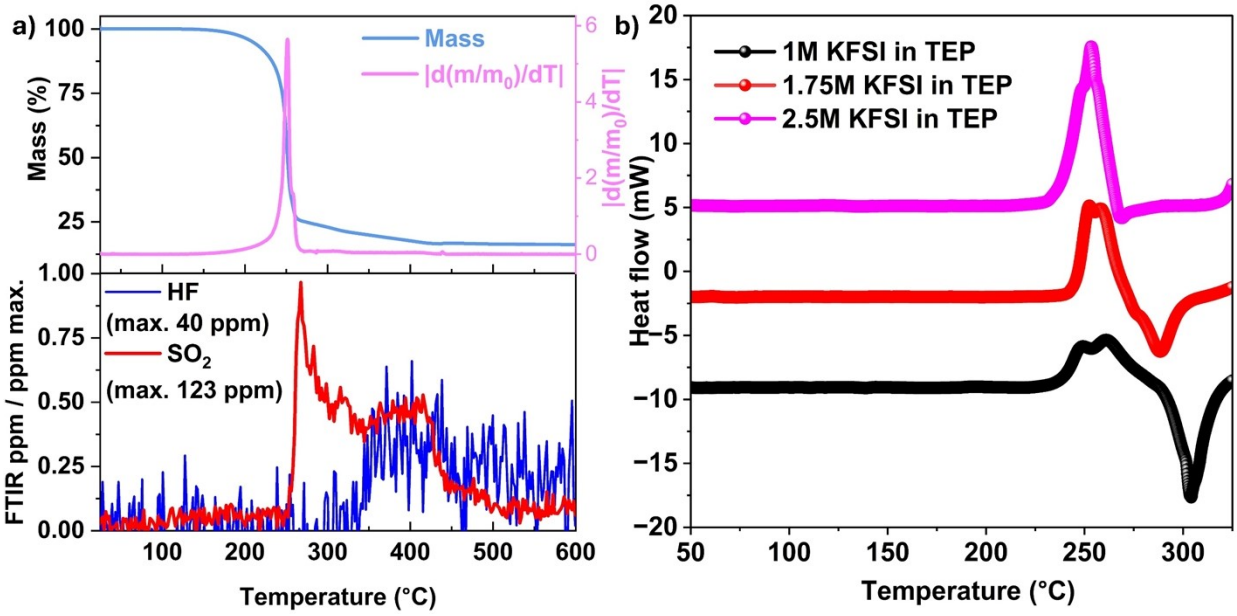

Figure S26. (a) TGA-FTIR quantification experiment for SO_2 and HF gas evolution, (b) HP-DSC measurements of KFSI in TEP electrolytes at salt concentrations of 2.5 M, 1.75 M, and 1.0 M.

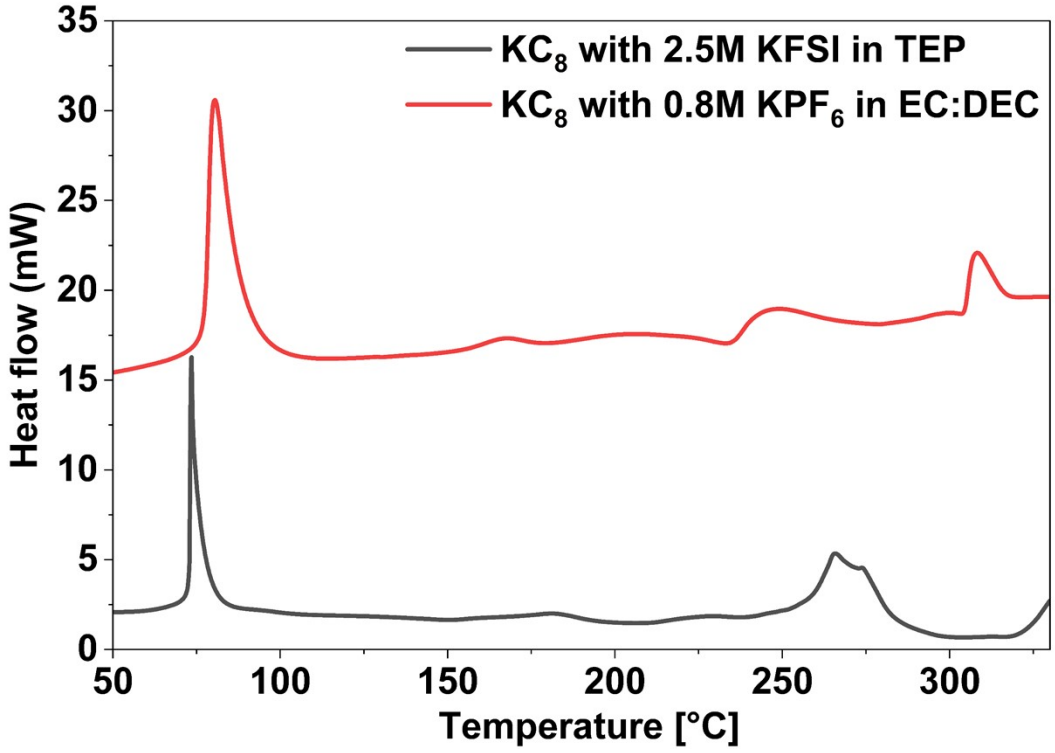

Figure S27. HP-DSC measurements for potassiated graphite (KC_8) in contact with 0.8 M KPF_6 in EC:DEC (1:1 by volume) and for comparison with 2.5 M KFSI in TEP.

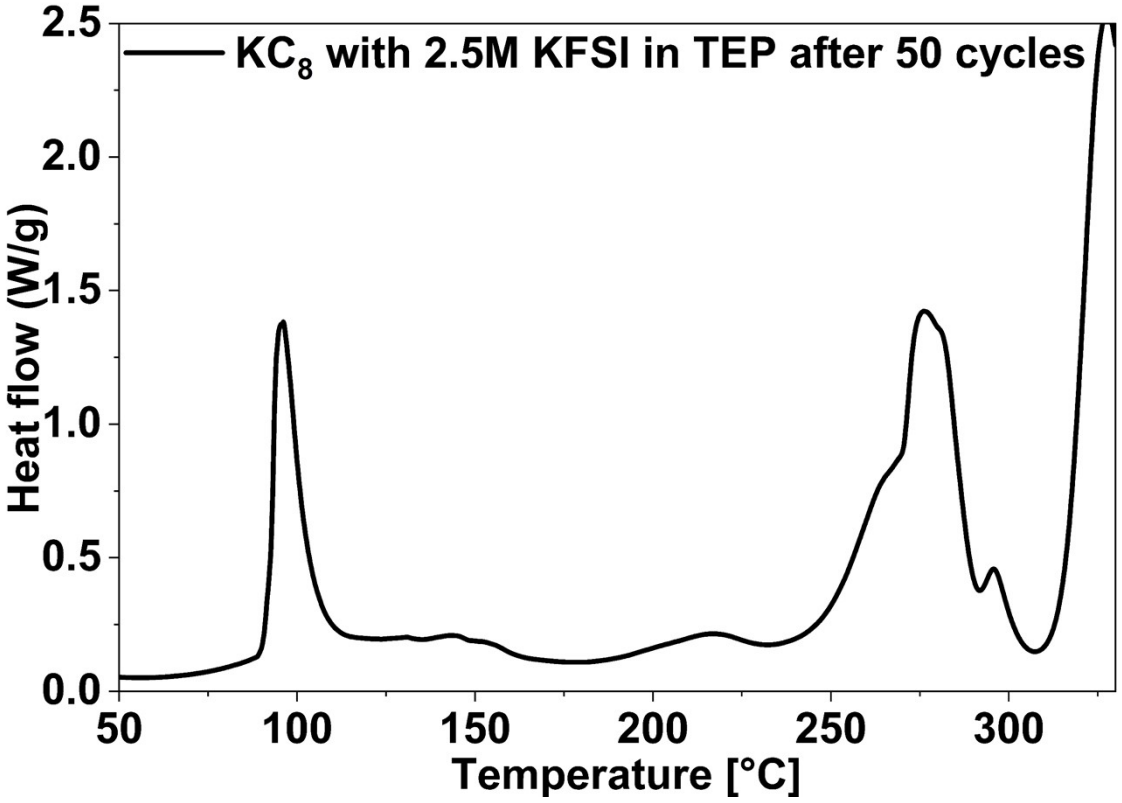

Figure S28. HP-DSC measurement on a fully charged (100% SOC) potassiated anode after 50 galvanostatic cycles, in contact with a 2.5 M KFSI–TEP electrolyte.

Table S1. XPS peak assignments for different elements based on literature references.

Elemental spectra	Binding energy (eV)	Component assignment	Ref.
C 1s	285	KC_8/ C-C	[6, 7]
	286.10	-C-O-	[7, 8]
	286.90	C-OH	[9]
	288.40	RCO_2Na	[9]
	288.60	K_2CO_3	[7, 8]
	289.80	Na_2CO_3	[9]
K 2p	292.86, 295.64	K-O/K-F	[7, 8, 10]
O 1s	530.40	K_2CO_3	[7, 8]
	531.00	RCO_2Na/Na_2CO_3	[9]
	531.40	-C-O-	[7, 8]
	532.70	O-P	[7]
	533.40	O=S=O (from FSI^-)	[8]
S 2p	161 - 164	$S/K_xS/K_2S$	[7, 11]
	166.38, 167.54	K_xSO_y	[7, 11]
	168.54, 169.70	$KSO_2F/KSNO_2F$/KFSI	[7, 8, 11]
F 1s	683.02, 684.00	K-F	[7, 8, 12]
	686.42, 687.21	P-F	[13, 14]
	688.15	S-F (from FSI^-)	[7, 8]
N 1s	398.02	$N\text{-}SO_x$	[11]
	399.66	$KNSO_2F$/KFSI	[11]
P 2p	133.11, 133.98	$(OEt)_xPO(OK)_{3-x}$	[15]
	134.93, 135.80	$K_xPO_yF_z$	[16]
	136.69, 137.56	$K_xPO_{y-a}(OEt)_aF_z$	[17]

Table S2. Percentage quantification of individual SEI species based on XPS analysis.

C 1s		**C-C**	**-C-O-**	**C-OH**	**RCO_2Na**	**K_2CO_3**	**Na_2CO_3**
	25 °C	61.04%	15.11%	3.90%	6.70%	7.62%	5.61%
	340 °C	71.11%	5.48%	2.74%	2.64%	16.80%	1.25%
	% change	+16.5%	–63.73%	–29.74%	–60.60%	120.5%	–77.72%
O 1s		**K_2CO_3**	**RCO_2Na/ Na_2CO_3**	**-C-O-**	**K_xSO_y**	**P-O**	**KFSI**
	25 °C	12.39%	4.95%	48.91%	4.18%	17.37%	12.20%
	340 °C	52.83%	2.17%	22.89%	9.86%	5.66%	6.59%
	% change	+326.4%	–56.16%	–53.2%	+135.9%	–67.4%	–45.98%
S 2p		**K_xS**	**K_xSO_y**	**KFSI**			
	25 °C	1.62%	17.32%	81.06%			
	340 °C	1.06%	41.05%	57.89%			
	% change	–34.57%	+137.01%	–28.58%			
N 1s		**$N\text{-}SO_x$**	**KFSI**				
	25 °C	63.45%	36.55%				
	340 °C	70.79%	29.21%				
	% change	+11.57%	–20.08%				
F 1s		**KF**	**S-F**	**P-F**			
	25 °C	45.90%	20.75%	43.35%			
	340 °C	38.70%	6.86%	54.41%			
	% change	–15.69%	–66.94%	+25.51%			
P 2p		**$K_xPO_{y-a}(OEt)_aF_z$**	**$K_xPO_yF_z$**	**$(OEt)_xPO(OK)_{3-x}$**			
	25 °C	50.95%	22.32%	26.73%			
	340 °C	40.08%	27.75%	32.19%			
	% change	–21.33%	+24.33%	+20.43%			

Note: All percentage changes are calculated relative to the atomic percentage at 25 °C. A "+" sign indicates an increase, while a "–" sign indicates a decrease.

Table S3. The assignments of selected secondary ions to corresponding SEI components.

SEI component assignment	**Secondary-ion fragments used**
KF, KFSI, and KFSI-derived products	KF^-
Carbonates (e.g., K_2CO_3)	KCO_3^-
Phosphates/fluorophosphates	KPO^- and PO_2^-
Sulfur/nitrogen oxy-species (e.g., $K[SO_x]$ and $K[NSO_x]$)	KS^-, KSO^-, and SNO^-
Binder-related organic fragments (CMC-Na)	$C_2H_3O^-$

Table S4. Exact values of net squared deviations for fragments at room temperature (RT), calculated in Igor Pro using the formula: $\sum_{(x,y)} (F_{map1} - F_{map2})^2$.

	K	F	KO	KF	KOF	^{34}S	KS	KSF	SO	KPO	KCO_3	CN	PO_2	SNO	MnF	MnS
K	0	13415.92	807.1815	1103.418	707.6625	1123.516	245.4128	2201.471	573.2325	3095.354	935.9696	8208.217	845.9696	994.7678	2556.356	5913.64
F	13415.92	0	19663.42	9381.443	17820.09	7468.059	10943.57	6157.244	16711.67	5270.449	14736.7	1647.295	10682.43	12509.16	5356.871	2807.554
KO	807.1815	19663.42	0	2570.132	179.0054	3275.226	1469.26	4579.726	252.2361	5911.942	954.9899	12833.28	2007.669	1388.201	5550.204	9830.828
KF	1103.418	9381.443	2570.132	0	2032.575	947.101	615.4371	1051.258	1784.97	1619.037	1460.958	5540.762	735.9296	912.2755	1453.691	3160.481
KOF	707.6625	17820.09	179.0054	2032.575	0	2696.683	1142.38	3627.268	81.60008	4979.254	738.3378	11457.42	1542.487	874.7633	4718.833	8643.155
^{34}S	1123.516	7468.059	3275.226	947.101	2696.683	0	524.9247	670.3679	2232.894	1134.654	2101.91	4052.589	784.4455	1465.657	744.3486	2693.62
KS	245.4128	10943.57	1469.26	615.4371	1142.38	524.9247	0	1213.975	902.8541	1940.416	1098.064	6594.498	496.2671	806.176	1511.672	4237.303
KSF	2201.471	6157.244	4579.726	1051.258	3627.268	670.3679	1213.975	0	3148.501	743.4502	2850.053	3615.788	1224.781	1738.521	642.0143	1826.591
SO	573.2325	16711.67	252.2361	1784.97	81.60008	2232.894	902.8541	3148.501	0	4490.525	702.9488	10616.51	1262.239	672.9341	4199.36	8022.425
KPO	3095.354	5270.449	5911.942	1619.037	4979.254	1134.654	1940.416	743.4502	4490.525	0	3535.189	3048.542	1639.767	2558.853	693.2956	1082.509
KCO_3	935.9696	14736.7	954.9899	1460.958	738.3378	2101.91	1098.064	2850.053	702.9488	3535.189	0	8716.44	987.1133	514.2587	3742.988	6315.386
CN	8208.217	1647.295	12833.28	5540.762	11457.42	4052.589	6594.498	3615.788	10616.51	3048.542	8716.44	0	6380.404	7384.017	3213.02	1906.699
PO_2	845.9696	10682.43	2007.669	735.9296	1542.487	784.4455	496.2671	1224.781	1262.239	1639.767	987.1133	6380.404	0	550.1087	1675.413	3835.645
SNO	994.7678	12509.16	1388.201	912.2755	874.7633	1465.657	806.176	1738.521	672.9341	2558.853	514.2587	7384.017	550.1087	0	2750.442	5074.786
MnF	2556.356	5356.871	5550.204	1453.691	4718.833	744.3486	1511.672	642.0143	4199.36	693.2956	3742.988	3213.02	1675.413	2750.442	0	1433.692
MnS	5913.64	2807.554	9830.828	3160.481	8643.155	2693.62	4237.303	1826.591	8022.425	1082.509	6315.386	1906.699	3835.645	5074.786	1433.692	0

Table S5. Exact values of net squared deviations for fragments at 340 °C, calculated in Igor Pro.

	K	F	KO	KF	KOF	^{34}S	KS	KSF	SO	KPO	KCO_3	CN	PO_2	SNO	MnF	MnS
K	0	7211.968	415.1704	446.4739	443.2415	153.2174	233.2981	349.9176	590.6353	1989.686	689.7859	5787.168	1623.922	1142.958	2198.814	979.7963
F	7211.968	0	10577.64	8222.53	9968.319	6499.212	5837.343	5909.494	11036.01	3651.967	4754.626	1022.951	2891.711	13090.49	3328.516	5830.326
KO	415.1704	10577.64	0	511.7362	107.7949	732.2167	943.4391	908.3922	74.00353	3466.354	1512.707	8767.423	3352.239	280.1946	3866.004	1721.143
KF	446.4739	8222.53	511.7362	0	362.8661	575.8429	591.3333	449.2441	553.0084	2323.444	915.6382	6723.822	2413.327	894.4376	2607.09	994.7125
KOF	443.2415	9968.319	107.7949	362.8661	0	626.69	810.4332	660.1376	67.19446	3043.036	1276.523	8277.753	3132.629	283.4512	3452.584	1411.653
^{34}S	153.2174	6499.212	732.2167	575.8429	626.69	0	124.5854	235.5931	815.9501	1467.109	651.3214	5229.889	1339.026	1410.124	1647.283	665.497
KS	233.2981	5837.343	943.4391	591.3333	810.4332	124.5854	0	164.0704	1099.687	1137.44	475.0511	4916.803	948.0652	1813.16	1189.923	495.7774
KSF	349.9176	5909.494	908.3922	449.2441	660.1376	235.5931	164.0704	0	981.8065	1139.827	324.3992	4905.221	1211.411	1628.53	1344.022	463.5538
SO	590.6353	11036.01	74.00353	553.0084	67.19446	815.9501	1099.687	981.8065	0	3684.681	1710.237	9177.996	3738.434	128.3833	4126.208	1837.311
KPO	1989.686	3651.967	3466.354	2323.444	3043.036	1467.109	1137.44	1139.827	3684.681	0	1012.433	3250.202	824.1872	4741.674	493.7409	816.5981
KCO_3	689.7859	4754.626	1512.707	915.6382	1276.523	651.3214	475.0511	324.3992	1710.237	1012.433	0	3888.01	951.0101	2547.763	1282.797	698.279
CN	5787.168	1022.951	8767.423	6723.822	8277.753	5229.889	4916.803	4905.221	9177.996	3250.202	3888.01	0	2691.776	10868.91	3261.184	4875.207
PO_2	1623.922	2891.711	3352.239	2413.327	3132.629	1339.026	948.0652	1211.411	3738.434	824.1872	951.0101	2691.776	0	4989.634	639.1993	1207.658
SNO	1142.958	13090.49	280.1946	894.4376	283.4512	1410.124	1813.16	1628.53	128.3833	4741.674	2547.763	10868.91	4989.634	0	5298.066	2484.198
MnF	2198.814	3328.516	3866.004	2607.09	3452.584	1647.283	1189.923	1344.022	4126.208	493.7409	1282.797	3261.184	639.1993	5298.066	0	996.2594
MnS	979.7963	5830.326	1721.143	994.7125	1411.653	665.497	495.7774	463.5538	1837.311	816.5981	698.279	4875.207	1207.658	2484.198	996.2594	0

Table S6. Exact values of relative correlation (in %) for fragments at room temperature (RT), calculated in Igor Pro using the formula:

$$\frac{100 \times \left(1 - \sum_{(x,y)} \left(F_{map1} - F_{map2}\right)^2\right)}{\sum_{(x,y)} \left(F_{map1} - F_{map2}\right)^2_{max}}\%$$

	K	F	KO	KF	KOF	^{34}S	KS	KSF	SO	KPO	KCO_3	CN	PO_2	SNO	MnF	MnS
K	100	31.77221	95.89501	94.38847	96.40112	94.28626	98.75193	88.80423	97.08478	84.25832	95.24004	58.25641	95.69775	94.94103	86.99944	69.92568
F	31.77221	100	0	52.28987	9.374393	62.02055	44.34552	68.68681	15.01139	73.19668	25.05528	91.62254	45.67358	36.38359	72.75717	85.72195
KO	95.89501	0	100	86.92938	99.08965	83.34356	92.52795	76.70941	98.71723	69.93431	95.14332	34.73526	89.78983	92.94019	71.77396	50.00449
KF	94.38847	52.28987	86.92938	100	89.66316	95.18343	96.87014	94.65374	90.92239	91.76625	92.57018	71.82198	96.25737	95.36054	92.60713	83.92711
KOF	96.40112	9.374393	99.08965	89.66316	100	86.28579	94.19033	81.55322	99.58501	74.67758	96.24512	41.73229	92.15555	95.55132	76.00197	56.0445
^{34}S	94.28626	62.02055	83.34356	95.18343	86.28579	100	97.33045	96.59079	88.64442	94.22962	89.31056	79.39021	96.01064	92.54628	96.21455	86.30137
KS	98.75193	44.34552	92.52795	96.87014	94.19033	97.33045	100	93.82623	95.40846	90.13185	94.4157	66.46312	97.47619	95.90012	92.31226	78.45084
KSF	88.80423	68.68681	76.70941	94.65374	81.55322	96.59079	93.82623	100	83.98803	96.21912	85.50581	81.6116	93.77127	91.15861	96.73499	90.71072
SO	97.08478	15.01139	98.71723	90.92239	99.58501	88.64442	95.40846	83.98803	100	77.16305	96.4251	46.00884	93.58078	96.57774	78.6438	59.20127
KPO	84.25832	73.19668	69.93431	91.76625	74.67758	94.22962	90.13185	96.21912	77.16305	100	82.0215	84.49638	91.66083	86.98673	96.47419	94.49481
KCO_3	95.24004	25.05528	95.14332	92.57018	96.24512	89.31056	94.4157	85.50581	96.4251	82.0215	100	55.6718	94.97995	97.3847	80.96471	67.88256
CN	58.25641	91.62254	34.73526	71.82198	41.73229	79.39021	66.46312	81.6116	46.00884	84.49638	55.6718	100	67.55191	62.44795	83.65991	90.30332
PO_2	95.69775	45.67358	89.78983	96.25737	92.15555	96.01064	97.47619	93.77127	93.58078	91.66083	94.97995	67.55191	100	97.20238	91.47955	80.4935
SNO	94.94103	36.38359	92.94019	95.36054	95.55132	92.54628	95.90012	91.15861	96.57774	86.98673	97.3847	62.44795	97.20238	100	86.01239	74.19174
MnF	86.99944	72.75717	71.77396	92.60713	76.00197	96.21455	92.31226	96.73499	78.6438	96.47419	80.96471	83.65991	91.47955	86.01239	100	92.70884
MnS	69.92568	85.72195	50.00449	83.92711	56.0445	86.30137	78.45084	90.71072	59.20127	94.49481	67.88256	90.30332	80.4935	74.19174	92.70884	100

Table S7. Exact values of relative correlation (in %) for fragments at 340 °C, calculated in Igor Pro.

	K	F	KO	KF	KOF	^{34}S	KS	KSF	SO	KPO	KCO_3	CN	PO_2	SNO	MnF	MnS
K	100	44.90683	96.82846	96.58933	96.61402	98.82955	98.2178	97.32694	95.48806	84.80053	94.73064	55.79107	87.59465	91.26879	83.20297	92.51521
F	44.90683	100	19.19603	37.18702	23.8507	50.35167	55.40777	54.8566	15.69449	72.10215	63.67879	92.18554	77.90984	0	74.57304	55.46138
KO	96.82846	19.19603	100	96.09078	99.17654	94.4065	92.79295	93.06068	99.43468	73.52007	88.44424	33.02451	74.39181	97.85956	70.46709	86.85196
KF	96.58933	37.18702	96.09078	100	97.22802	95.60106	95.48273	96.56817	95.7755	82.25091	93.00532	48.63585	81.56428	93.16727	80.0841	92.40126
KOF	96.61402	23.8507	99.17654	97.22802	100	95.21263	93.809	94.95712	99.48669	76.75385	90.24847	36.76516	76.06944	97.83468	73.62526	89.21619
^{34}S	98.82955	50.35167	94.4065	95.60106	95.21263	100	99.04828	98.20027	93.76685	88.79256	95.02447	60.04819	89.771	89.22788	87.41619	94.91618
KS	98.2178	55.40777	92.79295	95.48273	93.809	99.04828	100	98.74664	91.59935	91.31095	96.37103	62.4399	92.75761	86.14903	90.91002	96.21269
KSF	97.32694	54.8566	93.06068	96.56817	94.95712	98.20027	98.74664	100	92.49986	91.29271	97.52187	62.52837	90.74587	87.55945	89.73284	96.45886
SO	95.48806	15.69449	99.43468	95.7755	99.48669	93.76685	91.59935	92.49986	100	71.85224	86.93528	29.88808	71.44161	99.01926	68.47936	85.96454
KPO	84.80053	72.10215	73.52007	82.25091	76.75385	88.79256	91.31095	91.29271	71.85224	100	92.26589	75.17128	93.70393	63.77773	96.22825	93.7619
KCO_3	94.73064	63.67879	88.44424	93.00532	90.24847	95.02447	96.37103	97.52187	86.93528	92.26589	100	70.29898	92.73511	80.53731	90.20055	94.66576
CN	55.79107	92.18554	33.02451	48.63585	36.76516	60.04819	62.4399	62.52837	29.88808	75.17128	70.29898	100	79.43717	16.971	75.08739	62.75766
PO_2	87.59465	77.90984	74.39181	81.56428	76.06944	89.771	92.75761	90.74587	71.44161	93.70393	92.73511	79.43717	100	61.88353	95.11707	90.77454
SNO	91.26879	0	97.85956	93.16727	97.83468	89.22788	86.14903	87.55945	99.01926	63.77773	80.53731	16.971	61.88353	100	59.52738	81.02289
MnF	83.20297	74.57304	70.46709	80.0841	73.62526	87.41619	90.91002	89.73284	68.47936	96.22825	90.20055	75.08739	95.11707	59.52738	100	92.38944
MnS	92.51521	55.46138	86.85196	92.40126	89.21619	94.91618	96.21269	96.45886	85.96454	93.7619	94.66576	62.75766	90.77454	81.02289	92.38944	100

References

1. L. Deng, J. Qu, X. Niu, J. Liu, J. Zhang, Y. Hong, M. Feng, J. Wang, M. Hu and L. Zeng, *Nature communications*, 2021, **12**, 2167.
2. L. Lin, A. M. Yanyachi, J. E. Eichler, C. B. Mullins, D. P. Finegan and O. A. Ezekoye, *Energy Storage Materials*, 2025, 104313.
3. W. Li, U.-H. Kim, A. Dolocan, Y.-K. Sun and A. Manthiram, *ACS nano*, 2017, **11**, 5853–5863.
4. J. Zhao, B. Jagger, L. F. Olbrich, J. Ihli, S. Dhir, M. Zyskin, X. Ma and M. Pasta, *ACS Energy Letters*, 2024, **9**, 1537–1544.
5. J. Zhao, X. Zou, Y. Zhu, Y. Xu and C. Wang, *Advanced Functional Materials*, 2016, **26**, 8103–8110.
6. S. DiCenzo, S. Basu, G. Wertheim, D. Buchanan and J. Fischer, *Physical Review B*, 1982, **25**, 620.
7. H. Wang, J. Hu, J. Dong, K. C. Lau, L. Qin, Y. Lei, B. Li, D. Zhai, Y. Wu and F. Kang, *Advanced Energy Materials*, 2019, **9**, 1902697.
8. L. Caracciolo, L. Madec and H. Martinez, *ACS Applied Energy Materials*, 2021, **4**, 11693–11699.
9. A. Beda, S. Zallouz, S. Hajjar-Garreau, H. El Marouazi, L. Simonin and C. l. Matei Ghimbeu, *ACS Applied Materials & Interfaces*, 2024, **16**, 68664–68679.
10. A. Cano, L. Reguera, M. Avila, D. Velasco-Arias and E. Reguera, *European Journal of Inorganic Chemistry*, 2020, **2020**, 137–145.
11. X. Jiang, X. Liu, Z. Zeng, L. Xiao, X. Ai, H. Yang and Y. Cao, *Advanced Energy Materials*, 2018, **8**, 1802176.
12. H. Zhang, H. Wang, W. Li, Y. Wei, B. Wen, D. Zhai and F. Kang, *Advanced Functional Materials*, 2024, **34**, 2312368.
13. S. Moharana, G. West, A. S. Menon, W. L. da Silva, M. Walker and M. J. Loveridge, *ACS Applied Materials & Interfaces*, 2023, **15**, 50185–50195.
14. S. Ma, J. Zhao, H. Xiao, Q. Gao, F. Li, C. Song and G. Li, *Angewandte Chemie*, 2025, **137**, e202412955.
15. X. Jiang, X. Liu, Z. Zeng, L. Xiao, X. Ai, H. Yang and Y. Cao, *IScience*, 2018, **10**, 114–122.
16. D. Kim, S. Nanda, J. H. Kim, R. S. Monteiro, L. S. Parreira and H. Khani, *Journal of Materials Chemistry A*, 2025.
17. Y. Zhu, J. Mou, X. Gong, J. Wang, Q. Feng, X. Sun and Z. Liu, *Fuel*, 2025, **387**, 134456.